TOWARDS THE DEVELOPMENT OF A MULTI-SCALE MODEL FOR THERMALLY DRIVEN CIRCULATIONS

MD. ZAHANGIR HOSSAIN

Towards the development of a multi-scale model for thermally driven circulations

by

© Md. Zahangir Hossain
B. Sc.(Hons), M. Sc.

A thesis submitted to the
School of Graduate Studies
in partial fulfillment of the
requirements for the degree of
Master of Science.

Department of Mathematics & Statistics
Memorial University of Newfoundland

February 1, 2012

St. John's Newfoundland

Abstract

In this thesis, we have studied the development and assessment of a multi-scale Computational Fluid Dynamics (CFD) model for simulating thermally driven flows. Using a constant eddy viscosity model, mean momentum and energy equations, an urban heat island circulation is derived. To resolve the localized spatial features of such a circulation, we have studied the use of an adaptive mesh method based on wavelet transformation. We have proposed a second order fully implicit time integration scheme such that the momentum and the energy equations are solved simultaneously on an adaptive collocated grid. At each time step, a system of nonlinear equations is solved using a multi-scale method, where we have used a Krylov method for improving the rate of convergence, which is a distinct feature of the proposed CFD model. To the best of our knowledge, this is the first time attempt to use an adaptive mesh and a Krylov method to optimize a multi-scale solver for heat island circulation.

With a brief presentation of the scientific problem and the methodology in Chapters 1-3, the performance of the proposed model has been verified in Chapters 4-5, where we have simulated a shear-driven flow, a thermally driven natural convection flow, and a heat island circulation. We have found that our numerical results agree well with previously published benchmark simulation results of similar flows. First, the numerical error is proportional to the given tolerance. Second, a large CFL number does not affect the accuracy significantly. Finally, the computational cost grows linearly with the number of grid points if the mesh is refined locally. The proposed model is a novel contribution to the field of mesoscale meteorology, which would help for further development of multiscale meteorological modelling.

Acknowledgements

I would like to express my deepest gratitude to my supervisor, Dr. Jahrul Alam who made this work possible. This work would not be completed without his constant guidance, advice, patience and tremendous support. Special thanks goes to my supervisor for introducing me to such an interesting and challenging topic for my thesis. I am also grateful for his careful review of the manuscript.

I am grateful to the School of Graduate Studies and the Department of Mathematics and Statistics for providing financial support. I also acknowledge the Industrial Research and Innovation Fund (IRIF) program of the Government of Newfoundland and Labrador, and the Natural Sciences and Engineering Research Council (NSERC) of Canada for providing partial financial support as grants awarded to my supervisor.

Finally, and most importantly, I am grateful to my family, for their unflagging love, sacrifice and support throughout my life.

Contents

List of Tables

List of Figures

Abbreviations

UHI : Urban Heat Island

HI : Heat Island

CFD : Computational Fluid Dynamics

PDE : Partial Differential Equations

NSE : Navier-Stokes Equations

EI : Euler Implicit

EE : Euler Explicit

CN : Crank Nicolson

CFL : Courant Friedrichs Lewy condition

FTCS : Forward in Time and Centered in Space

BTCS : Backward in Time and Centered in Space

MPDE : Modified Partial Differential Equations

MAC : Marker and Cell

GMRES : Generalized Minimal Residual Method

FAS : Full Approximation Scheme

Nomenclature

u, v, w : Velocity component

x, y, z : Coordinate length

t : Time

p : Pressure

$\bar{p}(z)$: Hydrostatic pressure

p' : Non-hydrostatic pressure

ρ : Density

ρ' : Density perturbation

θ : Potential temperature

θ_0 : Background temperature

θ' : Temperature perturbation

$\bar{\theta}(z)$: Vertical temperature fluctuation

ν : Eddy viscosity

$\mathcal{V}$: Volume

β : Thermal expansion coefficient

κ : Thermal diffusivity

N : Buoyancy frequency

C_p : Specific heat at constant pressure

C_v : Specific heat at constant volume

L : Characteristic length scale

U : Characteristic velocity scale

Ra : Rayleigh number

Re : Reynolds number

Ri : Richardson number

Pr : Prandtl number

Fr : Froude number

$\mathcal{N}$: Number of adapted grid points

Δt : Time step

Δx : Grid spacing

ϵ : Tolerance

δ : Boundary layer width/solution of the linear system of equations

g : Gravitational acceleration

T : Temperature

Chapter 1

Introduction

In mesoscale meteorology, the study of thermally driven circulations has been an active area of research for the last century, and it is a subject of great interest to weather forecasters, research meteorologists, air quality scientists, and numerical modellers. Examples of mesoscale thermally driven motion include the sea- and land-breezes due to differential heating between the land and the ocean, formation of thunder storms, gravity current generation and propagation, and urban heat island circulations (e.g. see Lin, 2007).

Researchers in the field of atmospheric modelling debate the proper techniques for characterizing flow regimes; for example, whether a hydrostatic approximation is sufficient or a non-hydrostatic model must be used (e.g. see Martin & Pielke, 1983). Generally speaking, the air in the atmosphere is a compressible fluid, and hence, the compressible form of the governing equations are more appropriate for atmospheric modelling. Due to the propagation of sound waves, the numerical time integration of the compressible flow system requires extremely small time steps. It is often a question to understand the scales of atmospheric circulation, where an approximation to the scales of atmospheric circulation, where an approximation to the compressibility can

be adopted. In Fluid Dynamics, two approximations of a compressible system are common. The anelsatic approximation, in which the velocity field is not divergence free, perturbs the density field about a stationary reference state that varies both horizontally and vertically (Ogura & Phillips, 1962). The Boussinesq approximation, in which the velocity field is approximately divergence free, assumes that the change in density occurs due to a change in temperature, but neglects the variation of density except in the gravitational forcing terms (Spiegel & Veronis, 1960). Clearly, one may not be able to find a unique set of partial differential equations that can be solved numerically for the purpose of weather forecasting or projecting climate change. A more sophisticated and specific mathematical model as well as numerical methodology must be adopted, depending on the specific dynamics that need to be modelled.

In this thesis, we study the development of a computational model for simulating a thermally driven circulation that occurs naturally over the land. We also analyze the flow regime, in which such a computational model would compute approximately valid dynamics. First principle conservation laws will be used to derive a set of partial differential equations (PDEs) that models a class of thermally driven flows. Among mesoscale thermal circulations, urban heat island flows are of great importance in global warming and weather prediction, where a computational model may also be useful to explain observational information.

1.1 Urban heat island circulation in a large city

In fluid dynamics, a thermally driven circulation is often known as a convective flow. There are two basic types of convective flows: (i) natural convection, and (ii) forced convection (Bejan & Kraus, 2003). The main difference between a natural and a forced convection lies in the mechanism by which a flow is generated. If the motion of

the fluid occurs naturally due to a thermodynamic change in the absence of an external mechanical or hydrodynamical agent, the process is called natural convection. On the other hand, if the flow arises mainly due to an external agent, such as the wind or a fan, the process is called forced convection. If a forced convection occurs due to a pressure gradient force, we call this a pressure driven flow. A natural convection may also be classified as "convection," and a forced convection as "advection." The most common natural convections in engineering applications are mostly due to differential heating/cooling between two vertical planes, while the same in environmental applications are mostly due to differential or localized heating/cooling between two horizontal planes.

In environmental science, the urban heat island (UHI) is a phenomenon commonly observed in metropolitan areas, where the city center is significantly warmer than its surroundings (Kim & Baik, 2002). For example, Figure 1.1(a) shows a snapshot of the downtown area in the city of Toronto, ON, Canada. In other words, localized heating occurs between the earth's surface and an elevated horizontal surface. The phenomenon has been depicted schematically in Figure 1.1(b), which shows that the city's average surface temperature is highest in the downtown area. Such a temperature anomaly between the urban and suburban area, which also depends on urbanization, is roughly about 10° F or 6° C. The increased temperature in the downtown (*i.e.*, in the urban) area is associated mainly with human activities such as industries, construction of buildings, transportation etc. Observational studies indicate that the UHI may influence the local weather system significantly by increasing the average monthly rainfall, the frequency of cloud occurrence, and lightning (e.g. Baik *et al.*, 2001).

Since global temperature is measured in urban areas (*e.g.* near an airport), the UHI effect also accounts for predictions in the global warming trend. For example,

Yang *et al.* (2011) analyzed monthly mean surface air temperature data showing that UHI effects contribute about 24.2% to the regional average warming trend, and observed a significant effect of rapid urbanization on the surface air temperature after the early 2000s. Due to the importance of UHI in examining the environmental effect on weather, its basic dynamics have been studied since the beginning of the last century (e.g. see Delage & Taylor, 1970; Niino *et al.*, 2006).

1.1.1 A brief overview of urban heat island modelling

There is a growing scientific interest in the study of UHI effects due to its influence on precipitation and convection (e.g. Kim & Baik, 2002; Baik *et al.*, 2001). Niino *et al.* (2006) used numerical experiments as well as mathematical analysis to investigate the transition of different flow regimes of nonlinear heat island circulation, and agreed with the conclusions that were postulated previously by Kimura (1975) from laboratory experiments and numerical simulations. Baik & Chun (1997) investigated the effects of nonlinearity on the possible precipitation change downwind of the UHI by analytically solving the problem of the weakly nonlinear response of a stably stratified uniform flow to prescribed heating. Han & Baik (2008) studied urban heat island circulation and convection using a linear theory and a nonlinear numerical model. UHI circulation, in the absence of synoptic winds, has been investigated by Delage & Taylor (1970). Dubois & Touzani (2009) presented a basic computational fluid dynamics (CFD) model for simulating a steady state solution of a natural convection flow that represents an idealized two-dimensional heat island circulation.

The computational modelling of heat island circulation remains a difficult as well as an active area of research. Niino *et al.* (2006) provided a dimensional analysis that identifies flow regimes of a hydrostatic and those of non-hydrostatic limits. Dubois

& Touzani (2009) presented an idealized non-hydrostatic numerical model of two-dimensional heat island flow that requires a computational domain that is extremely large in the horizontal direction in order to simulate horizontally propagated circulation - known as the horizontal convection. The work of Dubois & Touzani (2009) indicates clearly that designing appropriate boundary conditions and numerical algorithms are notable difficulties in developing a non-hydrostatic model of heat island circulation. Moreover, obstacles or solid bodies (such as high-rise buildings) that block air circulation in urban areas, mean that modelling of UHI is as difficult as modelling fluid-structure interaction problems or bluff-body aerodynamics. In addition, there is a growing need for detailed simulation of turbulent structures above the UHI circulation in a stratified environment. The development of a fundamental numerical model of UHI circulation has not been sufficiently examined. For example, a model that simulates UHI circulation in the city of Toronto, ON, may not effectively simulate the conditions in St John's, NL, due to the widely varied character of these two cities, because computer models of UHI are often developed based on specific observational data analysis and *ad-hoc* mathematical assumptions.

1.2 Summary

This thesis extends the computational atmospheric modelling approach recently proposed by Alam (2011) to heat island circulations modelling. The main contribution of this thesis includes the following:

- A non-hydrostatic adaptive mesh model for heat island circulation is presented.
- The time step restriction due to adaptively refined spatial mesh is addressed, and a fully implicit time integration is studied for space-time adaptivity.

- A multi-scale algorithm for solving the nonlinear algebraic system due to implicit time integration is proposed and verified.

- The proposed model is verified with previously published benchmark simulation of forced convection, natural convection, and idealized heat island flows.

In Chapter 2, we present a mathematical model in which the density variation occurs mainly due to temperature variation which can represent heat island circulation adequately. The set of partial differential equations (PDE) is derived from first principles and has the form that is commonly used in CFD models. However, this form of the equations is normally not used to represent circulations in the atmosphere. The validity of these governing equations is studied as well. In Chapter 3, the time integration for an adaptive multi-scale numerical methodology is discussed briefly. This numerical model is verified in Chapter 4 by comparing numerical simulation results with previously published benchmark simulations. In Chapter 5, a heat island circulation is simulated, where the effect of various non-dimensional parameters is studied. Finally, in Chapter 6 the results are summarized with a discussion of future research directions.

(a)

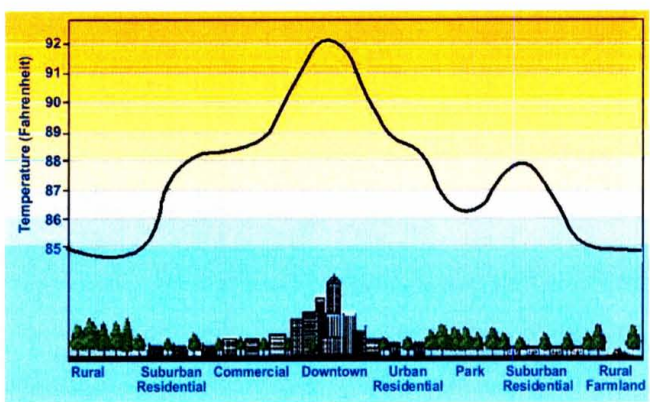

(b)

Figure 1.1: (a) A snapshot of downtown Toronto, showing the city center with high-rise buildings; (b) A schematic profile for the temperature distribution between urban and rural areas.

Chapter 2

Mathematical Model

This chapter presents the background and the general governing equations of thermally driven flows. The equation of thermally driven flows in the atmosphere is a set of partial differential equations (PDE) governed by the conservation laws of mass, momentum and energy. However, we need some basic assumptions to get a simplified mathematical model of the flow. The governing equations are converted to dimensionless form by choosing suitable characteristic scales.

2.1 Background

The air flow in the earth's atmosphere constitutes a compressible Fluid Dynamics system, and the fully compressible set of governing equations can be derived from first principles or conservation laws. In this chapter, we have adopted an approximation to the basic equations of a compressible flow. In our derivation, there are two fundamental principles. First, the effect of molecular viscosity has been neglected because the scale of viscous effect is much smaller than the resolved scale. Second, the assumption is that a fluctuation in the density field occurs due to the thermal effect

as opposed to the effect of pressure. In the latter case, a fully compressible model is needed. However, in the former case (thermal effect), the conservation laws for mass and momentum take an approximate form, where the density variation is contained in the forcing terms associated with the earth's gravitational field. In the study of thermal convection problems in CFD applications of engineering interests, this approach is commonly known as the Boussinesq approach. However, in the field of atmospheric modelling, the approximate conservation of mass takes two forms. In one form, the density field is perturbed over a slowly varying base state, which is known as the anelastic approximation (e.g. Ogura & Phillips, 1962). In the other form, the density field is perturbed over a base state such that the mass conservation is represented by a velocity field that is approximately divergence free. Mathematically, this form is similar to the classical Boussinesq approximation. A more detailed discussion using a formal dimensional analysis of the conservation laws is given by Pielke (2002).

2.2 An approximation to the conservation law of mass

The conservation of mass for a compressible flow is expressed by the partial differential equation,

$$\frac{\partial \rho}{\partial t} + \nabla \cdot (\rho \boldsymbol{u}) = 0, \tag{2.1}$$

where $\boldsymbol{u}$ is the velocity, ρ is the density and t is the time.

The fully compressible form (2.1) of the conservation of mass introduces a number of difficulties when we adopt a numerical modelling approach. Without providing a detailed discussion of a compressible model of the atmosphere, we want to study an approximate form of the mass conservation, where density is not a constant, but a

change in density occurs due to the change in temperature. As explained in Kundu & Cohen (2008), such an approximation is often known as the Boussinesq approximation, and is used commonly in the study of thermal convection (e.g. Spiegel & Veronis, 1960).

First, we note that introducing the notation

$$\frac{D}{Dt} = \frac{\partial}{\partial t} + \boldsymbol{u} \cdot \nabla,$$

and expanding the divergence term, equation (2.1) can be written as

$$-\frac{1}{\rho}\frac{D\rho}{Dt} = \nabla \cdot \boldsymbol{u}. \tag{2.2}$$

Equation (2.2) states that the fractional rate of change in the density field, $\frac{\frac{D\rho}{Dt}}{\rho}$, is equal in magnitude to the divergence of the velocity field. This means that if the density field varies only slowly; *i.e.*, $\left|\frac{1}{\rho}\frac{D\rho}{Dt}\right| \ll 1$, the velocity field is approximately divergence free. We can also see that the divergence of the velocity field accounts for the fractional rate of expansion of a material volume of fluid. In the study of atmospheric science, an alternative to the density field is the specific volume defined by

$$\mathcal{V} = \frac{1}{\rho},$$

where perturbation analyses are often done using the specific volume, $\mathcal{V}$, instead of the density field, ρ (Pielke, 2002). Following Batchelor (2000) and replacing $\mathcal{V}$ for ρ in equation (2.2), we can see that the relative change in the rate of specific volume is also related to divergence of the velocity field, i.e.

$$\frac{1}{\mathcal{V}}\frac{D\mathcal{V}}{Dt} = \nabla \cdot \boldsymbol{u}. \tag{2.3}$$

Equations (2.2) and (2.3) show that the fractional rate of change of density, and that of volume expansion of a material element of fluids are equal in magnitude.

To proceed further, let us now consider a dimensional analysis of equation (2.2), and use physical properties of the lower atmosphere to verify that the conservation of mass can be represented by the divergence free velocity field. We assume that U and L are characteristic scales for the velocity and the length respectively, and that the horizontal scale of circulation is much larger than the vertical scale of circulation. This means that the horizontal gradients of specific volume are negligible compared to its vertical gradient. As explained in Pielke (2002), the temporal variation in the basic state of the specific volume can also be neglected in dimensional reasoning. Using a typical scale $\Delta\rho$ for the density perturbation, we can write

$$\frac{D\rho}{Dt} \sim \frac{\Delta\rho U}{L}.$$

Hence

$$\frac{\frac{1}{\rho}\frac{D\rho}{Dt}}{\nabla \cdot \boldsymbol{u}} \sim \frac{\Delta\rho}{\rho} = -\beta\Delta T,$$

where β is known as the thermal expansion coefficient, and ΔT is the temperature perturbation corresponding to the density perturbation $\Delta\rho$. The last equality stems from the assumption that a change in density is the result of a change in temperature.

In the lower atmosphere, the thermal expansion coefficient, β is $\mathcal{O}(10^{-3}\ \mathrm{K}^{-1})$. Clearly, a temperature difference $\Delta T \sim 10$ K may introduce only a small fraction of density variation because

$$\frac{\Delta\rho}{\rho} \sim \beta\Delta T = \mathcal{O}(10^{-2}).$$

Observation of thermodynamic properties of the dry atmosphere indicates that at altitudes higher than about 8 km, the above estimate is fully violated. Using dimensional analysis, Pielke (2002) showed that the fractional rate of change of volume expansion is negligible if the vertical scale, L, of circulation is much smaller than the density scale height, *e.g.* 8 km. In such a circumstance, the divergence free velocity

field represents the conservation of mass sufficiently accurately, where the magnitude of the fractional change of density, $\frac{1}{\rho}\frac{D\rho}{Dt}$ and fractional change of volume, $\frac{1}{V}\frac{DV}{Dt}$ is very small in comparison to the magnitude of the velocity gradient, $\nabla \cdot \boldsymbol{u}$. In other words, a numerical model can be developed by replacing equation (2.2) with equation (2.4):

$$\boldsymbol{\nabla} \cdot \boldsymbol{u} = 0. \tag{2.4}$$

We also note that if $L = \mathcal{O}(8\text{km})$, equation (2.4) must be replaced with its anelastic form (e.g. Ogura & Phillips, 1962; Pielke, 2002). The approximate conservation of mass (2.4) is commonly used in the study of mesoscale meteorological phenomena (e.g. Pielke, 2002; Lin, 2007; Alam & Lin, 2008; Alam, 2011). For numerical modelling of mass conservation in thermally driven flows such as heat island circulation, the use of equation (2.4) is appropriate because the vertical scale of this circulation is much smaller than the density scale height of the atmosphere (e.g. Niino *et al.*, 2006).

2.3 Approximate conservation law for momentum transfer

Corresponding to the approximate mass conservation law for mesoscale atmospheric circulations, we need to obtain an approximation to the fundamental momentum conservation law. In vector form, the momentum conservation law in the atmosphere using a non-rotating frame of reference is given by

$$\rho\frac{D\boldsymbol{u}}{Dt} = -\nabla p + \boldsymbol{\nabla} \cdot \boldsymbol{\sigma} - \rho\boldsymbol{g}, \tag{2.5}$$

where p is the pressure and $\boldsymbol{\sigma}$ is the deviatoric stress tensor exerted in a material volume or parcel of fluid (Kundu & Cohen, 2008). Here, the effect of molecular viscosity is contained in the divergence term $\boldsymbol{\nabla} \cdot \boldsymbol{\sigma}$. Molecular interactions occur at a small

length scale that cannot be resolved in a numerical model when the characteristic length scale of the circulation is in the order of kilometres. Hence the stress term $\boldsymbol{\nabla} \cdot \boldsymbol{\sigma}$ is normally removed from the momentum equation (2.5).

Commonly, an approximation to the momentum conservation (2.5) is obtained by considering an average circulation so that the flow is resolved up to a certain scale, and the effects of the flows at smaller scales are modelled. This concept is the principal assumption that is used in the field of atmospheric modelling. However, the actual process of averaging differs in different applications. In the present work, we use this fundamental approach to derive a model that represents the circulation for a range of length scales. Let us consider the perturbation

$$\boldsymbol{u} = \boldsymbol{u}_0 + \boldsymbol{u}' + \boldsymbol{u}'', \tag{2.6}$$

where $\boldsymbol{u}$ represents a dependent variable such as u, v, w. Also define

$$\bar{\boldsymbol{u}} = \boldsymbol{u}_0 + \boldsymbol{u}'. \tag{2.7}$$

Hence

$$\boldsymbol{u} = \bar{\boldsymbol{u}} + \boldsymbol{u}''. \tag{2.8}$$

In this decomposition, $\boldsymbol{u}_0$ is a large scale reference state that can be considered as a synoptic scale value, $\boldsymbol{u}'$ is a resolvable small scale perturbation that covers scales smaller than the synoptic scale but larger than the scale that cannot be resolved in a numerical model, and $\boldsymbol{u}''$ is a smaller scale perturbation. With $\boldsymbol{u}_0$ being a synoptic scale reference value, $\boldsymbol{u}'$ can be considered a mesoscale perturbation that will be resolved in the numerical model. Furthermore, the mean of $\boldsymbol{u} = \bar{\boldsymbol{u}}$ and $\boldsymbol{u}'' = 0$. Symbolically $\langle \boldsymbol{u} \rangle = \bar{\boldsymbol{u}}$, $\langle \boldsymbol{u}'' \rangle = 0$.

When we substitute equation (2.8) into the momentum conservation law (2.5), where the molecular viscosity term $\boldsymbol{\nabla} \cdot \boldsymbol{\sigma}$ has been removed, and consider the average

or mean conservation law, *i.e.* $\langle$*equation* (2.5)$\rangle$, the nonlinear advection term takes the form

$$\langle \boldsymbol{u} \cdot \boldsymbol{\nabla} \boldsymbol{u} \rangle = \bar{\boldsymbol{u}} \cdot \boldsymbol{\nabla} \bar{\boldsymbol{u}} + \boldsymbol{f}(\bar{\boldsymbol{u}}, \boldsymbol{\nabla} \bar{\boldsymbol{u}}, \boldsymbol{u}'', \boldsymbol{\nabla} \boldsymbol{u}''),$$

where $\boldsymbol{f}$ is an unknown nonlinear function that represents the effect of the unresolved perturbation $\boldsymbol{u}''$. Without loss of generality, we can take $\boldsymbol{f} = \boldsymbol{\nabla} \cdot \boldsymbol{\sigma}$, where $\boldsymbol{\sigma}$ is an unknown vector valued function. Thus, the mean momentum equation retains its original form (2.5) with a term $\boldsymbol{\nabla} \cdot \boldsymbol{\sigma}$ that needs to be determined (for details, see Pielke, 2002, Ch.4).

In Newtonian Fluid Dynamics, the stress tensor is linearly proportional to the velocity gradient tensor, and the constant of proportionality accounts for the coefficient of molecular viscosity. This theory can be used to obtain an *ad-hoc* model for $\boldsymbol{\sigma}$. As described in Lin (2007) as well as in Kundu & Cohen (2008), instead of looking at the molecular interaction, we consider the interaction between parcels of fluid having vortical circulation; these parcels of fluid are often called eddies. In this case, the constant of proportionality accounts for the interaction between eddies, and is known as the eddy viscosity coefficient. In principle, this approach calculates only mesoscale eddies, and the effect of smaller eddies is approximated with an *ad-hoc* eddy viscosity model. The constant eddy viscosity model results in

$$\boldsymbol{\nabla} \cdot \boldsymbol{\sigma} = \mu \nabla^2 \boldsymbol{u},$$

where μ/ρ stands for the coefficient of eddy viscosity, which has a dimension $\mathrm{m^2 s^{-1}}$ that is the same as the dimension of kinematic viscosity. Here $\boldsymbol{u}$ is used instead of $\bar{\boldsymbol{u}}$ for simplicity. The typical suggested value for a vertical eddy viscosity coefficient is 10 $\mathrm{m^2 s^{-1}}$, which is much larger than the value of kinematic viscosity 10^{-6} $\mathrm{m^2 s^{-1}}$.

Suppose a density perturbation, $\rho = \rho_0 + \rho'$, where ρ_0 is the background density and $\rho\prime$ is the fluctuation over the background density. Substituting the perturbed

density, ρ, using the eddy viscosity model, and dividing both sides by ρ_0, equation (2.5) implies that

$$\left(1+\frac{\rho'}{\rho_0}\right)\frac{D\boldsymbol{u}}{Dt} = -\frac{1}{\rho_0}\nabla p + \frac{\mu}{\rho_0}\nabla^2\boldsymbol{u} - \left(1+\frac{\rho'}{\rho_0}\right)\boldsymbol{g}. \tag{2.9}$$

Let $p = \bar{p}(\boldsymbol{z}) + p'(\boldsymbol{x}, t)$, where $\bar{p}$ is the hydrostatic pressure and p' is the non-hydrostatic pressure. Applying hydrostatic balance

$$\frac{1}{\rho_0}\frac{\partial \bar{p}(\boldsymbol{z})}{\partial z} = -\boldsymbol{g}, \tag{2.10}$$

and subtracting equation (2.10) from equation (2.9) results in the momentum conservation law for a non-hydrostatic circulation,

$$\left(1+\frac{\rho'}{\rho_0}\right)\frac{D\boldsymbol{u}}{Dt} = -\frac{1}{\rho_0}\nabla p' + \frac{\mu}{\rho_0}\nabla^2\boldsymbol{u} - \frac{\rho'}{\rho_0}\boldsymbol{g}. \tag{2.11}$$

As presented in Section 2.2, the fractional change in the density field is given by $|\frac{\rho'}{\rho_0}| = \mathcal{O}(10^{-2}) \ll 1$; clearly, the density variation makes a small correction to the inertia term. This means that $\frac{\rho'}{\rho_0}\frac{D\boldsymbol{u}}{Dt}$ is a negligible correction of $\frac{D\boldsymbol{u}}{Dt}$ due to density change and can be neglected.

Hence,

$$\frac{D\boldsymbol{u}}{Dt} = -\frac{1}{\rho_0}\nabla p + \frac{\mu}{\rho_0}\nabla^2\mathbf{u} - \frac{\rho'}{\rho_0}\boldsymbol{g}. \tag{2.12}$$

The momentum conservation law for modelling thermally driven flows in a non-rotating frame is given by equation (2.12). This derivation explains why the density variation is neglected everywhere except at the gravitational forcing term.

2.4 Conservation of Energy

The principle for the conservation of energy is obtained from the first law of thermodynamics. The energy conservation law is reduced to an advection-diffusion equation

for the temperature. However, the potential temperature θ is the most appropriate quantity to describe temperature in the atmosphere. The potential temperature of a fluid parcel is the temperature that the fluid parcel would acquire if it were brought adiabatically to a standard pressure. Kundu & Cohen (2008) and Pielke (2002) have articulated details on how an equation for the potential temperature can be derived from first the principle. The mean energy conservation law is expressed by the partial differential equation,

$$\frac{\partial \theta}{\partial t} + \boldsymbol{u}.\nabla\theta = \kappa\nabla^2\theta, \tag{2.13}$$

where κ is the thermal diffusivity in the sense of an eddy viscosity model.

Suppose a temperature perturbation, $\theta = \theta_0 + \bar{\theta}(z) + \theta'(\boldsymbol{x}, t)$, where θ_0 is the background temperature, $\bar{\theta}(z)$ is the vertical fluctuation and θ' is the fluctuation over the background temperature. The temperature perturbation θ' can be expressed in terms of the density perturbation ρ' using the ideal gas law,

$$\frac{\theta'}{\theta_0} = \frac{C_v}{C_p}\frac{p'}{\bar{p}} - \frac{\rho'}{\rho_0}, \tag{2.14}$$

where C_p is the specific heat at constant pressure and C_v is the specific heat at constant volume. Assuming $|\frac{p'}{\bar{p}}| \ll 1$, the relation between density perturbation ρ' and temperature perturbation θ' is given by

$$\frac{\rho'}{\rho_0} \sim -\frac{\theta'}{\theta_0}. \tag{2.15}$$

In the field of atmospheric modelling, equation (2.15) couples the momentum equation (2.12) with the energy equation (2.16). Without going into the mathematical details, we can express the energy conservation law in terms of the perturbed temperature θ' by

$$\frac{\partial \theta'}{\partial t} + \boldsymbol{u}.\nabla\theta' + \frac{\partial \bar{\theta}}{\partial z}w = \kappa\nabla^2\theta'. \tag{2.16}$$

In this thesis, we will use equation (2.14) to model energy conservation law in terms of perturbation potential temperature θ'.

2.5 Governing equations of thermally driven flows

The governing equations for a three-dimensional thermally driven flow, representing a dry atmosphere at mesoscale using a non-rotating frame of reference, are given by the equations (2.4), (2.12), (2.15) and (2.16). These equations can be written in the scalar component form, where the prime ($'$) and the over bar ($\bar{}$) have been dropped for simplicity,

$$\frac{\partial u}{\partial x} + \frac{\partial v}{\partial y} + \frac{\partial w}{\partial z} = 0, \tag{2.17}$$

$$\frac{\partial u}{\partial t} + u\frac{\partial u}{\partial x} + v\frac{\partial u}{\partial y} + w\frac{\partial u}{\partial z} = -\frac{1}{\rho_0}\frac{\partial p}{\partial x} + \nu\left(\frac{\partial^2 u}{\partial x^2} + \frac{\partial^2 u}{\partial y^2} + \frac{\partial^2 u}{\partial z^2}\right), \tag{2.18}$$

$$\frac{\partial v}{\partial t} + u\frac{\partial v}{\partial x} + v\frac{\partial v}{\partial y} + w\frac{\partial v}{\partial z} = -\frac{1}{\rho_0}\frac{\partial p}{\partial y} + \nu\left(\frac{\partial^2 v}{\partial x^2} + \frac{\partial^2 v}{\partial y^2} + \frac{\partial^2 v}{\partial z^2}\right), \tag{2.19}$$

$$\frac{\partial w}{\partial t} + u\frac{\partial w}{\partial x} + v\frac{\partial w}{\partial y} + w\frac{\partial w}{\partial z} = -\frac{1}{\rho_0}\frac{\partial p}{\partial z} + \nu\left(\frac{\partial^2 w}{\partial x^2} + \frac{\partial^2 w}{\partial y^2} + \frac{\partial^2 w}{\partial z^2}\right) + \frac{\theta}{\theta_0}g, \tag{2.20}$$

$$\frac{\partial \theta}{\partial t} + u\frac{\partial \theta}{\partial x} + v\frac{\partial \theta}{\partial y} + w\frac{\partial \theta}{\partial z} + \frac{\partial \bar{\theta}}{\partial z}w = \kappa\left(\frac{\partial^2 \theta}{\partial x^2} + \frac{\partial^2 \theta}{\partial y^2} + \frac{\partial^2 \theta}{\partial z^2}\right), \tag{2.21}$$

where u, v, and w are velocity components, θ is the potential temperature, ρ is the fluid density, $\nu = \frac{\mu}{\rho_0}$ is the constant eddy viscosity in the present model, and κ is the constant thermal diffusivity.

For the purpose of developing a general numerical model that would simulate different flows, let us define the dimensionless form of the governing equations.

2.6 Dimensionless governing equations

For numerical solution, the dimensionless form of the governing equations of fluid flow is very important. After making the equations dimensionless we obtain some dimensionless parameters that are also very important for the explanation of flow regimes, the importance of the different terms and the effect of a given flow. There are some properties of the fluid dynamics system that can be observed without solving the system of equations by analyzing dimensionless parameters only.

We have non-dimensionalized the governing equations by using appropriate scales for the dependent and independent variables. For a natural convection flow, the length scale is L, and the time scale is L/U, where $U = \sqrt{g\beta L\Delta\theta}$ is the velocity scale, $\Delta\theta$ is a scale for the temperature, and β is the thermal expansion coefficient. The characteristic parameters for the dependent and independent variables that are used to make the governing equations dimensionless are listed in Table 2.1.

After making them dimensionless, the governing equations of the thermally driven flow are given by:

$$\frac{\partial u}{\partial x} + \frac{\partial v}{\partial y} + \frac{\partial w}{\partial z} = 0, \tag{2.22}$$

$$\frac{\partial u}{\partial t} + u\frac{\partial u}{\partial x} + v\frac{\partial u}{\partial y} + w\frac{\partial u}{\partial z} = -\frac{\partial p}{\partial x} + \sqrt{\frac{Pr}{Ra}}\left(\frac{\partial^2 u}{\partial x^2} + \frac{\partial^2 u}{\partial y^2} + \frac{\partial^2 u}{\partial z^2}\right), \tag{2.23}$$

$$\frac{\partial v}{\partial t} + u\frac{\partial v}{\partial x} + v\frac{\partial v}{\partial y} + w\frac{\partial v}{\partial z} = -\frac{\partial p}{\partial y} + \sqrt{\frac{Pr}{Ra}}\left(\frac{\partial^2 v}{\partial x^2} + \frac{\partial^2 v}{\partial y^2} + \frac{\partial^2 v}{\partial z^2}\right), \tag{2.24}$$

$$\frac{\partial w}{\partial t} + u\frac{\partial w}{\partial x} + v\frac{\partial v}{\partial y} + w\frac{\partial w}{\partial z} = -\frac{\partial p}{\partial z} + \sqrt{\frac{Pr}{Ra}}\left(\frac{\partial^2 w}{\partial x^2} + \frac{\partial^2 v}{\partial y^2} + \frac{\partial^2 w}{\partial z^2}\right) + Ri\ \theta, \tag{2.25}$$

$$\frac{\partial \theta}{\partial t} + u\frac{\partial \theta}{\partial x} + v\frac{\partial \theta}{\partial y} + w\frac{\partial \theta}{\partial z} + \frac{1}{Ri(Fr)^2}w = \frac{1}{\sqrt{RaPr}}\left(\frac{\partial^2 \theta}{\partial x^2} + \frac{\partial^2 \theta}{\partial y^2} + \frac{\partial^2 \theta}{\partial z^2}\right), \tag{2.26}$$

where the nondimensional parameters, Ra, Ri, Pr and Fr are defined in Table 2.2.

The above system of equations will be used in this thesis to represent mathematically a natural convection flow. However, all simulated flows that are presented in this

thesis are approximately two-dimensional, and hence the effect of the spatial derivative $\frac{\partial(\cdot)}{\partial y}$ has been neglected where appropriate. In order to solve these equations, we must consider appropriate boundary conditions and initial conditions. Since these conditions are different for different circulations, those are provided in the appropriate section, where a specific flow being simulated.

Variables	Scales
length(x, y, z)	L
velocity (u, v, w)	$U = \sqrt{g\beta L\Delta\theta}$
time (t)	L/U
pressure (p)	$\rho_0 U^2$
temperature (θ)	$\Delta\theta$
large scale ref. state density	ρ_0

Table 2.1: Scales of the dependent and independent variable.

Parameters name	Definition	Dimension
Rayleigh number, Ra	$\frac{\beta L^3 \Delta\theta}{\nu\kappa} g$	$\mathcal{O}(1)$
Richardson number, Ri	$\frac{\Delta\theta L}{\theta_0 U^2} g$	$\mathcal{O}(1)$
Prandtl number, Pr	$\frac{\nu}{\kappa}$	$\mathcal{O}(1)$
Froude number, Fr	$\frac{U}{LN}$	$\mathcal{O}(1)$
Buoyancy frequency, N	$\sqrt{\frac{g}{\theta_0}\frac{\partial\bar{\theta}}{\partial z}}$	$\mathcal{O}(s^{-1})$

Table 2.2: Definition of dimensional and dimensionless parameters.

2.7 Summary

In this chapter, we have explained briefly the approximate conservation laws of mass, momentum, and energy for thermally driven flows in the atmosphere. We have also presented the scales of dependent and independent variables, and the dimensionless form of the governing equations of thermally driven flows.

In the next chapter, we will discuss the numerical techniques for simulating thermally driven flows in atmospheric science.

Chapter 3

Numerical Methodology

In order to solve a system of partial differential equations numerically, we have to derive a discrete system of the given continuous equations. A system of prognostic equations (Alam & Lin, 2008; Alam, 2011) describing a thermally forced flow can be compactly written as

$$\frac{\partial \boldsymbol{\psi}}{\partial t} + \boldsymbol{u} \cdot \nabla \boldsymbol{\psi} = \boldsymbol{R}, \tag{3.1}$$

where $\boldsymbol{u}$ is the d-dimensional velocity vector, $\boldsymbol{\psi}$ is a vector of p ($p \geq d$) state variables including $\boldsymbol{u}$, and $\boldsymbol{R} = R(\psi)$ is a vector that represents all forces and source terms. Equation (3.1) is a compact representation of the conservation laws that were studied in Chapter 2. The vectors $\boldsymbol{u}$, $\boldsymbol{\psi}$ and $\boldsymbol{R}$ can be defined by

$$\boldsymbol{\psi} = [\psi_1, \psi_2, \ldots\ldots, \psi_p]^T,$$

$$\boldsymbol{u} = [u_1, u_2, \ldots\ldots, u_d]^T, \tag{3.2}$$

$$\boldsymbol{R} = [f_1(\psi), f_2(\psi), \ldots\ldots, f_p(\psi)]^T. \tag{3.3}$$

Consider the following 1D example, (3.1) can be written as

$$\frac{\partial u}{\partial t} + u\frac{\partial u}{\partial x} = \nu \frac{\partial^2 u}{\partial x^2}, \tag{3.4}$$

where

$$\boldsymbol{\psi} = [u],\ \mathbf{u} = [u] \text{ and } \mathbf{R}(\psi) = [\nu \tfrac{\partial^2 u}{\partial x^2}].$$

Consider another 1D example

$$\frac{\partial \omega}{\partial t} + u\frac{\partial \omega}{\partial x} = \nu \frac{\partial^2 \omega}{\partial x^2}, \tag{3.5}$$

$$\frac{\partial \theta}{\partial t} + u\frac{\partial \theta}{\partial x} = \kappa \frac{\partial^2 \theta}{\partial x^2}, \tag{3.6}$$

where

$$\boldsymbol{\psi} = [\omega, \theta]^T,\ \mathbf{u} = [u] \text{ and } \mathbf{R} = \left[\nu \tfrac{\partial^2 \omega}{\partial x^2}, \kappa \tfrac{\partial^2 \theta}{\partial x^2}\right]^T.$$

For 2D, equation (3.1) takes the form

$$\frac{\partial u}{\partial t} + u\frac{\partial u}{\partial x} + w\frac{\partial u}{\partial z} = \nu \left(\frac{\partial^2 u}{\partial x^2} + \frac{\partial^2 u}{\partial z^2}\right) + f_1(u, w), \tag{3.7}$$

$$\frac{\partial w}{\partial t} + u\frac{\partial w}{\partial x} + w\frac{\partial w}{\partial z} = \nu \left(\frac{\partial^2 w}{\partial x^2} + \frac{\partial^2 w}{\partial z^2}\right) + f_2(u, w) + g(\theta), \tag{3.8}$$

$$\frac{\partial \theta}{\partial t} + u\frac{\partial \theta}{\partial x} + w\frac{\partial \theta}{\partial z} = \kappa \left(\frac{\partial^2 \theta}{\partial x^2} + \frac{\partial^2 \theta}{\partial z^2}\right) + Q(u, w, \theta), \tag{3.9}$$

the vectors $\boldsymbol{\psi}$, $\boldsymbol{u}$ and $\boldsymbol{R}(\psi)$ are given by

$$\boldsymbol{\psi} = [u, w, \theta]^T,\ \boldsymbol{u} = [u, w]^T \text{ and}$$

$$\mathbf{R}(\psi) = \begin{bmatrix} \nu \left(\frac{\partial^2 u}{\partial x^2} + \frac{\partial^2 u}{\partial z^2}\right) + f_1(u, w) \\ \nu \left(\frac{\partial^2 w}{\partial x^2} + \frac{\partial^2 w}{\partial z^2}\right) + f_2(u, w) + g(\theta) \\ \kappa \left(\frac{\partial^2 \theta}{\partial x^2} + \frac{\partial^2 \theta}{\partial z^2}\right) + Q(u, w, \theta) \end{bmatrix}.$$

This chapter presents an efficient numerical methodology for solving equation (3.1).

3.1 An adaptive mesh approach for spatial discretization

There is a growing interest in using the adaptive mesh approach in the field of atmospheric modelling (e.g. see, Skamarock *et al.*, 1989; Jablonowski, 2004; Jablonowski *et al.*, 2004; Alam, 2011). A distinct feature of the present development is the use of an adaptive mesh methodology for computing multi-scale dynamics of thermally driven flows. In the present work, we aim to study how to extend an adaptive mesh approach for simulating two-dimensional thermally driven circulations. Detailed study of the present adaptive mesh technique were given by Vasilyev & Bowman (2000), Vasilyev & Kevlahan (2005), and Alam (2011). In this thesis, only additional study of those materials have been presented briefly, which we have studied for the purpose of the proposed multi-scale model.

For a brief description, let us consider a numerical solution $\mathbf{u}$ of any problem on a grid (e.g. a solution of (3.48)), and suppose that $\mathbf{d} = \mathbb{W}\mathbf{u}$ represents the wavelet transform of $\mathbf{u}$, where $\mathbb{W}$ denotes a wavelet transform operation. The wavelet transform $\mathbf{d}$ provides information on the local regularity of the corresponding solution. More specifically, only those grid points that are associated with large wavelet coefficients represent or approximate $\mathbf{u}$ numerically, where the number of such grid points is usually small if the solution $\mathbf{u}$ is highly localized. If the wavelet coefficients are filtered based on a tolerance ϵ, the error of such adaptivity remains $\mathcal{O}(\epsilon)$. The computational complexity of this adaptivity is $\mathcal{O}(\mathcal{N})$, where the number of the largest retained wavelet coefficient is $\mathcal{N}$. The *a priori* error control and the optimal computational complexity are promising properties of the wavelet based adaptive mesh methodology. Vasilyev & Kevlahan (2005) developed an algorithm to implement a wavelet based adaptive mesh method for solving linear elliptic PDEs.

If the method of Vasilyev & Kevlahan (2005) is used to develop an adaptive mesh method for solving time dependent advection-diffusion PDEs that are generally nonlinear, additional care must be taken to design a time integration scheme. This becomes more challenging in Fluid Dynamics, where the determination of the pressure gradient terms is an unresolved difficulty. Let us now present our analysis and development of a suitable time integration method so that an adaptive mesh methodology can be developed for solving (3.1).

3.2 Time discretization

In order to present the temporal discretization, let us denote the discrete time at n-th step by $t_n = n\Delta t$. Let us also use u_i^n to represent a function $u(x,t)$ at i-th grid point and at n-th time step. A numerical time integration method is generally called a time marching scheme because an approximate value of $u(x,t)$ at $(n+1)$-th time step, u_i^{n+1} is obtained using previously known approximation u_i^n. Since this thesis aims to study a computational model of thermally driven circulations, which is a convective phenomenon, we want to analyze and select an appropriate time marching scheme so that the time steps are not constrained by a stability restriction. To explain key properties -advantages/disadvantages - of classical time marching schemes, let us consider equation (3.4) as a simplified model of (3.1). Note that a conditionally stable scheme for (3.4) would reduce the time step whenever the mesh is refined, and this restriction is point-wise. In other words, the stability condition must be satisfied on each individual grid point. Such a stability condition must be addressed carefully since we have employed an adaptive mesh technique. For example, if the mesh has been refined only locally, the stability condition requires that the time step be reduced only on the refined mesh. However, a classical time marching scheme would reduce

the time step globally on both the fine and coarse grid points - even though the spatial mesh is refined only locally if a conditionally stable scheme is used.

Let us now present a basic time marching scheme for equation (3.4):

$$\left.\frac{\partial u}{\partial t}\right|_i^{n+1} + c\alpha \left.\frac{\partial u}{\partial x}\right|_i^{n+1} + c(1-\alpha)\left.\frac{\partial u}{\partial x}\right|_i^{n} = \nu\alpha \left.\frac{\partial^2 u}{\partial x^2}\right|_i^{n+1} + \nu(1-\alpha)\left.\frac{\partial^2 u}{\partial x^2}\right|_i^{n}, \tag{3.10}$$

where $\alpha \in \{0, \frac{1}{2}, 1\}$. Here, the scheme (3.10) is known as Euler explicit (EE), Crank-Nicolson (CN), or Euler implicit (EI) if $\alpha = 0, \frac{1}{2}$, or 1 respectively. The temporal discretization of PDE should be handled carefully, because the advection term described in the model equations may introduce an unexpected instability in the numerical scheme. Let us now study the stability conditions of the implicit and explicit schemes.

3.3 Explicit and implicit schemes

In order to study stability conditions and long time behaviour of the solutions of explicit and implicit schemes we consider equation (3.4), which is known as one dimensional Burger's equation, as a simplified model of (3.1). Let us now study the temporal discretization scheme of the Burger's equation (3.4). For $\alpha = 0$, the EE scheme (3.10) takes the form

$$\left.\frac{\partial u}{\partial t}\right|_i^{n+1} + c\left.\frac{\partial u}{\partial x}\right|_i^{n} = \nu\left.\frac{\partial^2 u}{\partial x^2}\right|_i^{n}. \tag{3.11}$$

Discretizing the spatial derivative with the upwind method for the advection term and the central difference method for the diffusion term, equation (3.11) gives

$$\frac{u_i^{n+1} - u_i^n}{\Delta t} + c\frac{u_i^n - u_{i-1}^n}{\Delta x} = \nu\frac{u_{i+1}^n - 2u_i^n + u_{i-1}^n}{(\Delta x)^2}, \quad c > 0 \tag{3.12}$$

$$\frac{u_i^{n+1} - u_i^n}{\Delta t} + c\frac{u_{i+1}^n - u_i^n}{\Delta x} = \nu\frac{u_{i+1}^n - 2u_i^n + u_{i-1}^n}{(\Delta x)^2}, \quad c < 0. \tag{3.13}$$

Here Δt is the time step and Δx is the grid spacing. It is first order accurate in both time and space, and conditionally stable. There is a time step restriction for the stability condition. However, we do not need to solve any algebraic system. Discretizing the spatial derivatives with centered in space gives

$$\frac{u_i^{n+1} - u_i^n}{\Delta t} + c\frac{u_{i+1}^n - u_{i-1}^n}{2\Delta x} = \nu\frac{u_{i+1}^n - 2u_i^n + u_{i-1}^n}{(\Delta x)^2}. \tag{3.14}$$

It is also called a forward in time and centered in space (FTCS) scheme that is first order in time and second order in space, and is also conditionally stable. There is also no need to solve an algebraic system.

Now using $\alpha = 1$ in (3.10), the EI scheme takes the form,

$$\left.\frac{\partial u}{\partial t}\right|_i^{n+1} + c\left.\frac{\partial u}{\partial x}\right|_i^{n+1} = \nu\left.\frac{\partial^2 u}{\partial x^2}\right|_i^{n+1}. \tag{3.15}$$

Discretizing the spatial derivatives with centered in space gives

$$\frac{u_i^{n+1} - u_i^n}{\Delta t} + c\frac{u_{i+1}^{n+1} - u_{i-1}^{n+1}}{2\Delta x} = \nu\frac{u_{i+1}^{n+1} - 2u_i^{n+1} + u_{i-1}^{n+1}}{(\Delta x)^2}. \tag{3.16}$$

It is also called a backward in time and centered in space (BTCS) scheme that is first order in time and second order in space. The BTCS scheme is unconditionally stable, but needs to solve a system of algebraic equations at each time step. Note that the FTCS scheme is conditionally stable, which requires a small Δt, and needs more CPU time. On the other hand the BTCS scheme may use large Δt, but also requires large CPU time because of the algebraic system.

The accuracy of the BTCS method can be improved by using $\alpha = \frac{1}{2}$ in (3.10). Using $\alpha = \frac{1}{2}$ in (3.10), the CN scheme takes the form

$$\left.\frac{\partial u}{\partial t}\right|_i^{n+1} + \frac{c}{2}\left(\left.\frac{\partial u}{\partial x}\right|_i^{n+1} + \left.\frac{\partial u}{\partial x}\right|_i^{n}\right) = \frac{\nu}{2}\left(\left.\frac{\partial^2 u}{\partial x^2}\right|_i^{n+1} + \left.\frac{\partial^2 u}{\partial x^2}\right|_i^{n}\right). \tag{3.17}$$

Discretizing the spatial derivatives with centered in space yields

$$\frac{u_i^{n+1}-u_i^n}{\Delta t}+\frac{c}{2}\left(\frac{u_{i+1}^{n+1}-u_{i-1}^{n+1}}{2\Delta x}+\frac{u_{i+1}^n-u_{i-1}^n}{2\Delta x}\right)= \frac{\nu}{2}\left(\frac{(u_{i+1}^{n+1}-2u_i^{n+1}+u_{i-1}^{n+1}}{(\Delta x)^2}+\frac{u_{i-1}^n-2u_i^n+u_{i-1}^n}{(\Delta x)^2}\right). \tag{3.18}$$

The CN scheme is implicit, second order in both space and time. One may use the Von Neumann method to find the stability condition of EE, EI and CN schemes. According to the Von Neumann method, the EE scheme is conditionally stable, but both the EI and CN schemes are unconditionally stable. In this thesis, we study a heuristic stability theory, to analyze a numerical scheme for CFD applications. This heuristic method is useful to understand stability as well as the accumulation of time integration errors. Let us now explain the stability of the above schemes using the heuristic method.

3.3.1 The method of heuristic stability analysis

To the best of our knowledge, the heuristic stability analysis method appeared in Warming & Hyett (1974) for the first time, and further details of this method were also discussed by Tannehill *et al.* (1997) in the context of CFD applications. The method aim to obtain an equivalent PDE from the numerical scheme, which is known as the modified partial differential equation (MPDE).

To explain briefly, let us find the MPDE for the scheme (3.12). In order to obtain the MPDE, the numerical approximations u_i^{n+1}, u_i^n, u_{i-1}^n, and u_{i+1}^n in the scheme (3.12) are replaced with their corresponding exact values $u\left(x_i,t_{n+1}\right)$, $u\left(x_i,t_n\right)$, $u\left(x_{i-1},t_n\right)$, and $u\left(x_{i+1},t_n\right)$. One may consider $\nu=0$, for simplicity, to get

$$\frac{u(x_i,t_{n+1})-u(x_i,t_n)}{\Delta t}+c\frac{u(x_i,t_n)-u(x_{i-1},t_n)}{\Delta x}=0. \tag{3.19}$$

Using Taylor series expansion with respect to (x_i, t_n), the algebraic equation (3.19) can be converted into the following partial differential equation

$$u_t + cu_x = \frac{c\Delta x}{2}\left(1 - \frac{c\Delta t}{\Delta x}\right) u_{xx} + O\left((\Delta x)^2, \Delta x \Delta t, (\Delta t)^2\right). \tag{3.20}$$

As discussed in Warming & Hyett (1974), the equation (3.20) is called the MPDE of (3.19). The heuristic method states that the numerical scheme would solve equation (3.20) instead of solving the actual PDE (3.4) with $\nu = 0$. Hence the numerical solution would behave like the solution of the MPDE, which is the key concept in this heuristic stability analysis method.

The heuristic stability theory states that a scheme is stable if

$$(-1)^{k-1} C_{2k} > 0,$$

where C_{2k} represents the efficient of the lowest order i.e. leading order even derivative error term of the MPDE (Warming & Hyett, 1974). If the leading order error term of the MPDE contains an even derivative, then the resulting error is called a dissipative error, and the numerical solution behaves like a "diffusion phenomenon." On the other hand, if the leading order error term is an odd derivative, then the resulting error is called dispersive error. We refer to the work of Warming & Hyett (1974) for a discussion on higher order terms. We can see this by ignoring all higher order terms from the right hand side of (3.20) as well as the advection term from the left hand side, and by looking at the time evolution of a single Fourier mode, $\hat{u}(t)$. When the second order even derivative term on the right hand side has a negative coefficient, each Fourier mode will grow, thereby leading to an unstable solution. Clearly, the solution of the MPDE (3.20) will be stable if the coefficient of the term with the second order derivative is positive, when all other higher order terms are neglected. In other words, we must have

$$0 \leq \frac{c\Delta t}{\Delta x} \leq 1. \tag{3.21}$$

Note that the condition (3.21) that is obtained from the MPDE is the same as the CFL condition that one would obtain from the Von Neumann stability analysis. The leading order error term in the truncation error contains the even derivative, hence the MPDE is useful to understand that the solution has dissipative error. With heuristic analysis, we not only understand the stability but also understand the long time behaviour of the solution. This analysis, in particular, is well suited for an adaptive mesh method, where Δx is a variable with respect to grid points.

The explicit FTCS scheme (3.14) is first order in time and second order in space. Using Von Neumann stability analysis we can easily observe that the FTCS scheme is unconditionally unstable if $\nu = 0$. The source of numerical instability may be identified using the Heuristic stability analysis proposed by Warming & Hyett (1974). In a similar manner the modified equation of the FCTS scheme (3.14) is given by

$$u_t + cu_x = -\frac{c^2 \Delta t}{2} u_{xx} + O\left((\Delta t)^2, (\Delta x)^2\right). \tag{3.22}$$

According to the Heuristic stability analysis, the FTCS scheme is unconditionally unstable because the coefficient of the leading order second derivative term on the right hand side is negative. Hence the first order explicit scheme is conditionally stable and the second order explicit scheme is unconditionally unstable for equation (3.4) with $\nu = 0$.

This analysis shows that the choice of an explicit scheme is not appropriate for simulating thermally driven circulation when advection or convection is a dominant phenomenon.

To explain further, let us now consider the scheme (3.12) or (3.14) for $c = 0$, *i.e.* the modified equation of the heat equation is given by

$$u_t - \nu u_{xx} = \left(-\frac{1}{2}\nu^2 \Delta t + \frac{\nu \Delta x^2}{12}\right) u_{xxxx} + O\left((\Delta x)^2, \Delta t (\Delta x)^2, (\Delta x)^4\right). \tag{3.23}$$

The scheme is stable if $0 \leq \frac{\nu \Delta t}{(\Delta x)^2} \leq \frac{1}{2}$, which makes the coefficient of the leading order error term positive. The leading order error term in the truncation error is an even derivative, so the solution has dissipative error.

However, the stability condition states that if Δx is reduced by a factor of q, then Δt must at least be reduced by a factor of q^2. For an adaptive mesh refinement mesh approach, the scheme would require an extremely small time step.

Furthermore, the modified equation of the FTCS scheme (3.14) for $c \neq 0$ is given by

$$u_t + cu_x = \left(\nu - \frac{c^2 \Delta t}{2}\right) u_{xx} + O\left((\Delta t), (\Delta)^2, (\Delta x)^2\right). \tag{3.24}$$

Here, we can compare (3.24) with (3.22). We see that in the absence of a diffusion term *i.e.* with $\nu = 0$ the FTCS scheme is unconditionally unstable, but in the presence of a diffusion term, the scheme becomes conditionally stable. This indicates how the eddy viscosity model is useful in a numerical model of fluid motion. However, equation (3.24) states that $\Delta t < \frac{2\nu}{c^2}$. Thus, despite the FTCS scheme being stable according to mathematical analysis, it is still not useful in a CFD model because ν is often very small, *i.e.* $\mathcal{O}(10^{-6})$.

Let us now discuss the stability conditions of the implicit scheme. The modified equation of the BTCS scheme (3.16) for $\nu = 0$, *i.e.* the MPDE of the wave equation is given by

$$u_t + cu_x = \frac{c^2 \Delta t}{2} u_{xx} + O\left((\Delta t)^2, (\Delta x)^2\right). \tag{3.25}$$

Again the modified equation of the BTCS scheme (3.16) for $c = 0$, *i.e.* the MPDE of the heat equation is given by

$$u_t - \nu u_{xx} = \left(\frac{\nu^2 \Delta t}{2} + \frac{\nu (\Delta x)^2}{12}\right) u_{xxxx} + \ldots\ldots \tag{3.26}$$

As the coefficient of the leading order error term of equation (3.25) and equation (3.26) is always positive, both the schemes are unconditionally stable. The leading order

error term in the truncation error contains an even derivative for both equations. The BTCS scheme is $\mathcal{O}(\Delta t, (\Delta x)^2)$ and unconditionally stable but it suffers from dissipative error.

The modified equation of the BTCS scheme (3.16), *i.e.* the MPDE of the Burger's equation is given by

$$u_t + cu_x = \left(\nu + \frac{c^2\Delta t}{2}\right) u_{xx} + O\left((\Delta t), (\Delta t)^2, (\Delta x)^2\right). \tag{3.27}$$

Therefore, we can compare the approach between (3.27) and (3.24). As the coefficient of the leading order error term is positive and contains an even derivative, the scheme is unconditionally stable and the solution contains dissipative error. The larger the Δt, the higher the dissipative effect.

In order to improve the scenario, consider the CN scheme (3.17) with $\nu = 0$ for simplicity, where the MPDE is given by

$$u_t + cu_x = -\left(\frac{c^3(\Delta t)^2}{12} + \frac{c(\Delta x)^2}{6}\right) u_{xxx} + O\left((\Delta t)^4, (\Delta t)^2(\Delta x)^2, (\Delta x)^4\right). \tag{3.28}$$

The leading order error term of the truncation error contains an odd derivative, so the solution has only dispersive error. Further, the modified equation of the scheme (3.17) for $c = 0$, *i.e.* the MPDE of the heat equation is given by

$$u_t - \nu u_{xx} = \frac{\nu(\Delta x)^2}{12} u_{xxxx} + O\left((\Delta t)^2, (\Delta x)^4\right). \tag{3.29}$$

However, comparison between (3.29) and (3.26) shows that the dissipation error in a CN scheme depends only on Δx. Hence the accuracy can be controlled by adaptive mesh refinement. Moreover, the advection term does not introduce any dissipative error.

This analysis does not fully explain how the dissipation error can be controlled by the adaptive mesh refinement approach without controlling the time step. We

agree that a suitable time-space adaptive method is needed. Clearly, there is no time step control in the CN scheme. Advanced analysis of this MPDE method for a fully non-linear equation remains an active area in numerical analysis.

Following this analysis, we have informed researchers in the field of atmospheric modelling on how to select a scheme so that the solution remains acceptable after a long time in a physical sense. In the present work, we have adopted the CN scheme for solving the fully nonlinear conservation laws, which is motivated from the above analysis. We will also discuss how to solve the resulting nonlinear system efficiently.

3.4 The proposed numerical algorithm

Applying the fully implicit CN scheme, the discretization for equation (3.1) subject to equation (2.4) is given by

$$\frac{\boldsymbol{\psi}^{n+1}-\boldsymbol{\psi}^{n}}{\Delta t}+\frac{1}{2}\left(\boldsymbol{u}^{n+1}\cdot\nabla\boldsymbol{\psi}^{n+1}+\boldsymbol{u}^{n}\cdot\nabla\boldsymbol{\psi}^{n}\right)=\frac{1}{2}\left(\boldsymbol{R}^{n+1}+\boldsymbol{R}^{n}\right), \tag{3.30}$$

$$\boldsymbol{\nabla}\cdot\boldsymbol{u}^{n+1}=0. \tag{3.31}$$

Using $\boldsymbol{\psi}=\boldsymbol{u}$ and the CN scheme (3.30), the NSE takes the form

$$\frac{\mathbf{u}^{n+1}-\mathbf{u}^{n}}{\Delta t}+\frac{1}{2}\left((\mathbf{u}^{n+1}\cdot\nabla)\mathbf{u}^{n+1}+(\mathbf{u}^{n}\cdot\nabla)\mathbf{u}^{n}\right)= -\nabla p^{n+1}+\frac{1}{2Re}\left(\nabla^{2}\mathbf{u}^{n+1}+\nabla^{2}\mathbf{u}^{n}\right) \tag{3.32}$$

$$\nabla\cdot\mathbf{u}^{n+1}=0. \tag{3.33}$$

In order to solve the above system, one main difficulty is pressure calculation, as there is no dynamical equation for pressure. The most commonly used methods for pressure calculation are Marker and Cell (MAC), and the Projection method.

3.4.1 The MAC method of Harlow and Welch(1965)

Harlow & Welch (1965) developed a method for solving the incompressible Navier-Stokes equations (NSE) (3.32)-(3.33). This method is also commonly referred to as the Marker and Cell (MAC) method. The MAC method is based on the staggered grid, where the pressure is computed on the cell center, and the velocity components are on the cell interfaces. The temporal discretization of the original MAC method adopts an explicit treatment of advection, pressure gradient, and diffusive terms. The solution is calculated by using the pressure from the previous time step, where pressure is calculated from the Poisson equation. In the original MAC method, the equation (3.32) was obtained using Euler explicit method.

$$\frac{\mathbf{u}^{n+1}-\mathbf{u}^{n}}{\Delta t}+(\mathbf{u}^{n}\cdot\nabla)\mathbf{u}^{n}=-\nabla p^{n}+\frac{1}{Re}\nabla^{2}\mathbf{u}^{n}, \tag{3.34}$$

$$\nabla\cdot\mathbf{u}^{n+1}=0. \tag{3.35}$$

Taking the divergence of the equation (3.34) yields

$$\frac{\nabla\cdot\mathbf{u}^{n+1}-\nabla\cdot\mathbf{u}^{n}}{\Delta t}+\nabla\cdot((\mathbf{u}^{n}\cdot\nabla)\mathbf{u}^{n})=-\nabla^{2}p^{n}+\frac{1}{Re}\nabla^{2}(\nabla\cdot\mathbf{u}^{n}). \tag{3.36}$$

Assume that the initial velocity field satisfies the divergence free condition, i.e. $\nabla\cdot\mathbf{u}^{n}=0$, then the equation (3.36) reduces to

$$\frac{\nabla\cdot\mathbf{u}^{n+1}}{\Delta t}+\nabla\cdot((\mathbf{u}^{n}\cdot\nabla)\mathbf{u}^{n})=-\nabla^{2}p^{n}. \tag{3.37}$$

In order to satisfy the divergence free condition $\nabla\cdot\mathbf{u}^{n+1}=0$, for the computed velocity field $\mathbf{u}^{n+1}$, it requires that

$$\nabla^{2}p^{n}=-\nabla\cdot\left((\mathbf{u}^{n}\cdot\nabla)\mathbf{u}^{n}\right), \tag{3.38}$$

which is the required Poisson equation for pressure. Using the Crank-Nicolson method for the viscous term and an explicit method for the advection term, the MAC method

retains the same Poisson equation for pressure calculation. From the MAC method, we see that (i) the grid is staggered (ii) the velocity field is divergence free i.e. $\nabla \cdot \mathbf{u}^{n+1} = 0$ at each time step, (iii) the pressure p is obtained explicitly from the explicit velocity field, and (iv) the nonlinear term is treated explicitly but the viscous term may be treated implicitly. Since the MAC method treats the advection term explicitly, it must always satisfy the CFL condition.

3.4.2 Projection method

Chorin (1968) developed a method for solving incompressible NSE, which is referred to as the projection method. This method is also known as the fractional step method, and was formulated on the regular (nonstaggered) grid (Tannehill *et al.*, 1997). It is an implicit method, so there is no stability condition or time step restriction. However, it requires solving two algebraic systems for the velocity field $\mathbf{u}^{n+1}$, and the pressure p^{n+1} at each time step, which is highly cost effective. The main advantage of the projection method is the application of a time-splitting discretization scheme that decouples the computation of velocity field and pressure, instead of satisfying the momentum equation and the divergence free condition simultaneously (E & Liu, 1995). In the first step, compute an intermediate velocity u^* by ignoring the divergence free condition and the pressure gradient term from the momentum equation. Therefore equation (3.32) gives

$$\frac{\mathbf{u}^* - \mathbf{u}^n}{\Delta t} + \frac{1}{2}\left((\mathbf{u}^* \cdot \nabla)\mathbf{u}^* + (\mathbf{u}^n \cdot \nabla)\mathbf{u}^n\right) = \frac{1}{2Re}\left(\nabla^2 \mathbf{u}^* + \nabla^2 \mathbf{u}^n\right). \tag{3.39}$$

In the second step, obtain the pressure p^{n+1} and the velocity field $\mathbf{u}^{n+1}$ by using the intermediate velocity u^* for the space of the divergence free vector field. The pressure is obtained by considering

$$\frac{u^{n+1} - u^*}{\Delta t} = -\nabla p^{n+1}, \tag{3.40}$$

and taking the divergence of equation (3.40), i.e.

$$\frac{\nabla \cdot u^{n+1} - \nabla \cdot u^{\star}}{\Delta t} = -\nabla^2 p^{n+1}. \tag{3.41}$$

In order to satisfy the divergence free condition $\nabla \cdot u^{n+1} = 0$, for the computed velocity field u^{n+1}, we now solve

$$\nabla^2 p^{n+1} = \frac{1}{\Delta t} \nabla \cdot u^{\star}, \tag{3.42}$$

for computing $u^{n+1} = u^{\star} - \Delta t \nabla p^{n+1}$. This approach requires an iterative method for a large algebraic system.

Here, we need to solve the non-linear equation (3.39) and the linear equation (3.42) at each time step. In this thesis we study the development of a nonlinear solver for solving (3.39). Let us now briefly introduce our approach in this direction.

3.5 Iterative methods for a linear system

In order to present our methodology for solving systems of algebraic equations, let us begin with iterative methods for a linear system. In this thesis, we use both the stationary and the non-stationary iterative methods. Suppose that

$$Ax = b, \tag{3.43}$$

is a given $n \times n$ linear system of equations, which can also be written as

$$\sum_{j=1}^{n} a_{ij} x_j = b_i, \quad i = 1, 2, 3, \ldots\ldots, n. \tag{3.44}$$

An iterative method aims to calculate the error e, so that an approximate solution x^k of (3.43) is corrected according to

$$x^{k+1} = x^k + e,$$

where the integer k refers to an iteration step (Barrett *et al.*, 2002). We will discuss in the next section that the above iterative approach remains the same, regardless of whether the given system is linear or nonlinear. There are several methods to determine the error e. When the error is small, we must have either $||x^{k+1} - x^k||_p \leq \delta$ or $||r||_p \leq \delta$, where $\delta > 0$ is a small number, and the residual r is defined by $r = b - Ax^k$. This is known as the convergence criterion or the stopping condition. Note that the required number of iterations for convergence depends mainly on the properties of A, and a theoretical development is not the purpose of this thesis.

A stationary iterative method aims to calculate e such that $x^k + e = Mx^k + c$, where M is a matrix and c is a vector. Thus, we get

$$x^{k+1} = Mx^k + c.$$

We will show that the matrix M needs to be defined directly, but the vector c can be ignored. Commonly used stationary methods for CFD applications are the Jacobi and Gauss-Seidel methods (Kelly, 1995).

3.5.1 Jacobi method

The naive iterative method for solving a linear system of equations is probably the Jacobi method, which is named for the German mathematician Carl Gustav Jacob Jacobi (Press *et al.*, 2007). The iteration matrix M can be found by using an additive splitting of the given matrix: $A = B + D + U$, where the matrix D contains the diagonal elements of A, B contains the lower-diagonal elements and U contains the upper-diagonal elements . We can write

$$x^{k+1} = \underbrace{-D^{-1}(B+U)}_{M} x^k + \underbrace{D^{-1}b}_{c}.$$

Using the form (3.44), we get

$$x_i^{(k+1)} = \frac{1}{a_{ii}} \left(b_i - \sum_{j \neq i} a_{ij} x_j^{(k)} \right), \quad i, j = 1, 2, 3, \ldots\ldots, n. \tag{3.45}$$

Using the matrix form, we can also write

$$\mathbf{x}^{(k+1)} = \mathbf{x}^{(k)} + D^{-1} \left(\mathbf{b} - A\mathbf{x}^{(k)} \right). \tag{3.46}$$

In this last form (3.46), we can see that the error e is given by $e = D^{-1} \left(\mathbf{b} - A\mathbf{x}^{(k)} \right)$, and no information about M and c is required.

Clearly, starting with an initial guess, each equation of the system is solved only for the corresponding element of the solution vector, keeping all other elements unchanged, thereby finding an updated approximation of the solution. The updated solutions are used for the next iteration. The process continues until the desired convergence criterion has been satisfied.

3.5.2 Gauss-Seidel method

The Gauss-Seidel iterative method of solving a linear system of equations aims to improve the rate of convergence of the Jacobi method. In this method, the most current approximate values of the solutions are used in each of the subsequent calculations. The Jacobi iteration (3.45) can be modified to obtain the Gauss-Seidel iteration

$$x_i^{(k+1)} = \frac{1}{a_{ii}} \left(b_i - \sum_{j<i} a_{ij} x_j^{(k+1)} - \sum_{j>i} a_{ij} x_j^{(k)} \right), \quad i, j = 1, 2, 3, \ldots\ldots, n,$$

which can be expressed using a matrix notation as

$$\mathbf{x}^{(k+1)} = \mathbf{x}^{(k)} + (D + L)^{-1} \left(\mathbf{b} - A\mathbf{x}^{(k)} \right). \tag{3.47}$$

In this case, the error e is calculated as $e = (D + B)^{-1} \left(\boldsymbol{b} - A\mathbf{x}^{(k)} \right)$.

From the above discussion, we see clearly that one needs to calculate the error e sequentially using a stationary iterative method until the desired convergence has been reached. However, the rate of convergence depends on the method of computing e as well as on the properties of the matrix A. For example, the matrix A needs to be diagonally dominant or symmetric and positive definite for the convergence of both the Jacobi and Gauss-Seidel iterations. The Gauss-Seidel method often requires fewer iterations than the Jacobi method to produce the same degree of accuracy.

In practice, one notices that the error often decreases very quickly by a certain factor during the first few iterations, and afterwards, the rate of convergence slows down. This happens particularly for most CFD applications where the Poisson or Helmholtz like equations are solved. For this reason, we cannot consider Jacobi or Gauss-Seidel method as the technique to solve most CFD applications (Tannehill *et al.*, 1997).

3.5.3 Krylov method

Krylov method is a non-stationary iterative method that is used to solve large and sparse linear systems, if the coefficient matrix, A of the system $Ax = b$ exists implicitly (van der Vorst, 2003). A Krylov method solves the system (3.43) by repeatedly performing matrix-vector multiplications involving A. Starting with an initial guess x_0, it gives more accurate approximations x_k to a desired solution. In iteration k, a Krylov method produces an approximate solution x_k from a Krylov space generated by the vector $r_0 = b - Ax_0$ (Ipsen & Meyer, 1998),

$$K_k(A, r_0) = \text{span}\{r_0, Ar_0, A^2r_0, \ldots\ldots, A^{k-1}r_0\}.$$

An example of a Krylov method is the generalized minimal residual method(GMRES), which was published by Saad & Schultz (1986). The GMRES method finds an ap-

proximate solution $x^k = x_0 + z^k$ from the Krylov space $K_k(A, r_0)$ so that the residual is as small as possible over the space; i.e. x_k solves the least square problem $\min_{z \in K_k} \|r^{(0)} - Az\|_2$, in the Euclidean norm $\|.\|_2$.

3.6 Iterative method for a nonlinear system

The nonlinear system of PDE gives a nonlinear system of equations after discretization. The solution of a non-linear system is more difficult than a linear one.

3.6.1 Newton method

In order to solve the nonlinear system of equations iteratively, we consider the Newton iteration scheme based on linearization of the problem. Using the current approximation of the solution and solving the linear system of equations that arises from the linearization, involving a Jacobian matrix, one determines the next approximation (Leveque, 2007). The solution of the linear system arising from the Newton iteration can be obtained from any one of the above methods. Consider nonlinear system of equations

$$L(\mathbf{u}) = 0, \tag{3.48}$$

where L is a nonlinear function. Supposing $\mathbf{u}^k$ is an approximate solution of (3.48), the Newton iteration is given by

$$\mathbf{u}^{k+1} = \mathbf{u}^k + \delta, \tag{3.49}$$

where δ is the solution of the linear system

$$J^k \delta = -L(\mathbf{u}^k), \tag{3.50}$$

here J^k is the Jacobian of the nonlinear system. In order to solve the nonlinear system of equations (3.48) for each outer or global iteration we have to solve a linear system

of equations (3.50) with some inner or local iterations. Therefore, the accuracy of the solution for (3.48) may depend on how accurately the linear system (3.50) has been solved. The linear system of equations (3.50) can be solved using any one of the methods discussed in section 3.5. In most of the CFD applications, the system of equations is very large. Therefore, the application of a method *e.g.* Jacobi, Gauss-Seidel or Krylov, for solving a large linear system of equations is expensive, because the CPU time increases drastically. However, we are seeking an efficient method for solving this type of large system of equations so that the computational cost is $\mathcal{O}(\mathcal{N})$. In other words, the cost remains proportional to the number of grid points $\mathcal{N}$.

In order to optimize the rate of convergence, we have developed a multilevel algorithm on an adaptive mesh, which has $\mathcal{O}(\mathcal{N})$ complexity.

3.7 An optimized multilevel method for non-linear problems

The multigrid method is an efficient and popular iterative algorithm for solving a large linear system of equations. The main advantage of this method is that, employing grids of different mesh levels, it provides rapid convergence, *i.e.* the convergence rate is often independent of the size of the discretized system (Jones & Woodward, 2000). Iterative relaxation is applied for smoothing of the error. A coarse grid correction is used, in which the smooth error is determined on a coarser grid. This error is interpolated to the fine grid, and is used to correct the fine-grid approximation.

For nonlinear problems, the Full Approximation Scheme (FAS) is an extension to the linear multigrid algorithm that needs an appropriate relaxation scheme for smoothing the error. The present nonlinear algorithm is similar to what was devel-

oped in Alam (2011). The same algorithm has been adapted to thermally driven circulation. One main technical difference includes the use of a restarted GMRES approach for smoothing the nonlinear system. Although the development and verification of a solution method for nonlinear flow problems is one significant contribution of this thesis, we have not provided a detailed description, to keep the thesis compact. Briefly, the algorithm takes advantages of the Krylov method, FAS method, and wavelet transform in the way these informations are presented in section 3.5 and 3.6. Note however that we have not introduced the wavelet transform method in this thesis.

3.8 Summary

In this chapter, we have briefly introduced the numerical methodology. The proposed method aims to take advantages of powerful but independent techniques - Krylov method, FAS method, and wavelet method - in order to develop a new computational model for fluid flow simulation. We have presented our analysis towards the need of developing this new technique.

We have presented the heuristic stability analysis, showing why and how a finite difference scheme may become useful or useless for CFD applications. This analysis is not a familiar approach in the field of atmospheric modelling. We have also discussed the difference between MAC and the projection method and analyzed why the projection method is more applicable if an adaptive mesh is used.

This numerical methodology is verified by simulating a shear driven flow as well as a natural convection flow in the next chapter.

Chapter 4

Model Verification

This chapter presents the performance of the proposed adaptive mesh model. In order to verify the model, two types of flow have been considered, (i) lid driven cavity flow and (ii) thermally driven cavity flow. Since these flows are commonly used for verification of CFD codes, the results are useful to understand computational benefits of the present work.

4.1 Lid-driven cavity flow

The lid-driven cavity flow is a classical test problem that is often used for the assessment of a new Computational Fluid Dynamics algorithm. Botella & Peyret (1998) computed benchmark solutions of the lid driven cavity flow for Reynolds number 10^3 using a Chebyshev collocation method. Ghia *et al.* (1982) studied the effectiveness of the multigrid method for high Re flow, where the fine mesh solutions of lid-driven flow in a square cavity have been obtained for Reynolds numbers up to 10^4 and meshes consisting of as many as 257×257 points. Bruneau & Saad (2006) studied 2D lid-driven cavity flow for various Reynolds numbers and provided benchmark results

for steady and periodic solutions. Peng *et al.* (2003) observed the direct numerical solution about the transition process from laminar to chaotic flow in square lid-driven cavity flows.

In Chapter 2, we have defined the velocity scale $U = \sqrt{g\beta L\Delta\theta}$, and obtained a dimensionless set of equations for coupled heat and mass transfer phenomena. We see that $\sqrt{\frac{Pr}{Ra}} = \frac{\nu}{UL} = \frac{1}{Re}$, where U can be considered a typical characteristic velocity scale, which is independent of $\Delta\theta$ for $Ri = 0$. Hence, the equations of two dimensional lid-driven cavity flow can be derived from the three dimensional equations (2.22 - 2.25), using $\frac{\partial}{\partial y}(\cdot) = 0$, $v = 0$ and $Ri = 0$ such that

$$\frac{\partial u}{\partial x} + \frac{\partial w}{\partial z} = 0, \tag{4.1}$$

$$\frac{\partial u}{\partial t} + u\frac{\partial u}{\partial x} + w\frac{\partial u}{\partial z} = -\frac{\partial p}{\partial x} + \frac{1}{Re}\left(\frac{\partial^2 u}{\partial x^2} + \frac{\partial^2 u}{\partial z^2}\right), \tag{4.2}$$

$$\frac{\partial w}{\partial t} + u\frac{\partial w}{\partial x} + w\frac{\partial w}{\partial z} = -\frac{\partial p}{\partial z} + \frac{1}{Re}\left(\frac{\partial^2 w}{\partial x^2} + \frac{\partial^2 w}{\partial z^2}\right), \tag{4.3}$$

where u and w are the velocity components in the horizontal and vertical directions respectively, p is the pressure, and $Re = \frac{UL}{\nu}$ is the Reynolds number.

4.1.1 Geometry and boundary conditions

Let us assume that the fluid is contained in a square domain, $\Omega = [0, 1] \times [0, 1]$ with known flow conditions on all sides. Normally one side is kept moving so that the fluid inside the container is driven by a shear stress. The geometry and boundary conditions are shown in Figure 4.1. Boundary conditions for the velocity field are the moving lid velocity at the top wall and no-slip conditions for the velocity components at the bottom wall and two side walls. The fluid inside the cavity is initially at rest. Therefore the boundary conditions are:

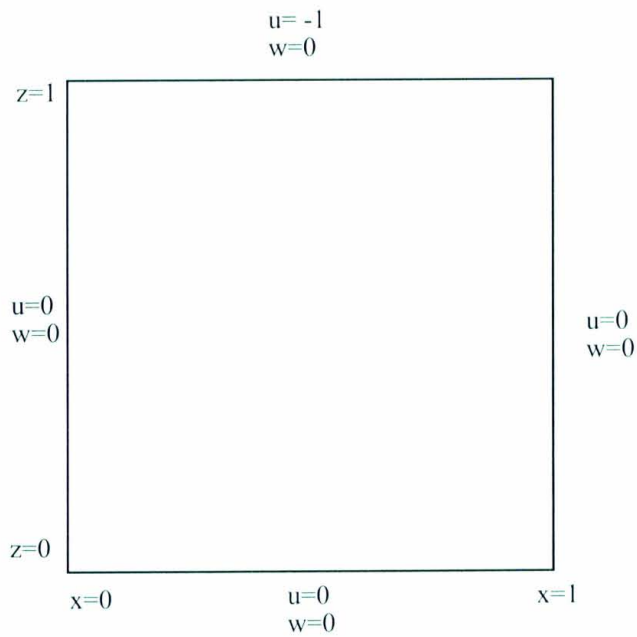

Figure 4.1: Lid-driven cavity flow configuration, and boundary conditions. The top wall moves at a dimensionless constant speed. All other walls are fixed with respect to the coordinate system.

$$u = -1,\ w = 0 \text{ at } z = 1,$$
$$u = w = 0 \text{ at } z = 0,\ x = 0, \text{ and } x = 1,$$
$$u = w = 0 \text{ at } t = 0, \forall (x, y) \in \Omega.$$

The proposed fully implicit adaptive multilevel method has been applied to simulate the lid driven cavity flow in order to test the numerical accuracy and the effectiveness of the model.

4.1.2 Reference numerical results

The numerical model was described by Botella & Peyret (1998) and Ghia *et al.* (1982), which is considered as a reference model. The governing equations of the reference model are also given by the equations (4.1-4.3). The boundary conditions and the problem geometry of the reference model are the same as discussed in section 4.1.1. Thus, the equations, boundary conditions, and parameters of the reference model are the same as those we have considered in this section.

4.1.3 Numerical results

The time dependent equations (4.1-4.3) have been solved using the proposed method, where the boundary conditions were interchanged so that any of the four boundaries moved at a constant speed. For a fixed Re, we have 8 numerical experiments, depending on the choice of the moving boundary and the moving direction. These experiments provide a good cross checking for numerical error, and results from one of these experiments have been presented with boundary conditions, as described in Figure 4.1.

The horizontal velocity fields for $Re = 10^3$ at $t = 40$, 45, and 50 are shown in Figure 4.2. Clearly, we see that the velocity field has reached a steady state; *i.e.* the

velocity field does not change significantly if time, t, is increased. At low Re, such a shear driven flow has a steady state solution, which means that the numerical method has computed the solution of the PDEs. The horizontal velocity profiles, $u(0.5, z)$, along a vertical line at $x = 0.5$ for resolution 160×160 and $Re = 10^3$ are shown in Figure 4.3. The comparison of the present result with the corresponding numerical data presented in Ghia *et al.* (1982) is shown in Figures 4.3(a), and the comparison with the corresponding numerical data presented in Botella & Peyret (1998) is shown in Figure 4.3(b). From Figures 4.3(a) and 4.3(b), we observe that the present result is in good agreement with the reference result.

Let us present the vertical velocity field (w) for $Re = 10^3$ at $t = 40$, 45, and 50 in Figure 4.4. The vertical velocity profiles, $w(x, 0.5)$, along a horizontal line at $z = 0.5$ for resolution 160×160 and $Re = 10^3$ are shown in Figure 4.5. The comparison of the present result with the corresponding numerical data presented in Ghia *et al.* (1982) is shown in Figures 4.5(a), and comparison with the corresponding numerical data presented in Botella & Peyret (1998) is shown in 4.5(b). From Figures 4.5(a) and 4.5(b), we observe that the present result is in good agreement with the reference results.

4.1.3.1 Space and time adaptivity

The spatial mesh is adapted based on the tolerance ϵ that is used to filter wavelet transform coefficients. One promising advantage of the wavelet based technique is that the wavelet transform identifies the grid points that are statistical outliers. In other words, discarding those grid points that are marked as outliers according to a given criterion, the computed solution that is obtained among the remaing grid points will retain an accuracy based on the tolerance. It has been shown from mathematical analysis as well as from numerical experiments that the error of such a wavelet filtering

is $O(\epsilon)$. Figure 4.6(a) shows the horizontal velocity through the vertical centre line of the cavity for $Re = 10^3$, and for $\epsilon = 10^{-2}$, 10^{-3}, 10^{-4}, 10^{-5}, 10^{-6}. The number of grid points corresponding to different values of ϵ are also given in Table 4.1. Clearly, the number of grid points increases if ϵ decreases. The result, presented in Figure 4.6(a) shows that the boundary layer is resolved accurately despite a large error tolerance ϵ or if a small number of grid points being used.

Moreover, in our adaptive mesh approach, we need only 3,416 (for $\epsilon = 10^{-3}$) grid points out of 160×160, which is about 5.2% compared to the grid points used in Ghia *et al.* (1982), and about 13.34% compared to what was used in Botella & Peyret (1998). From this comparison it is apparent that the numerical results are in good agreement with the reference solutions, despite using a small number of grid points.

ϵ	Grid points
10^{-2}	995
10^{-3}	3416
10^{-4}	10275
10^{-5}	21871
10^{-6}	25434

Table 4.1: Number of grid points as a function of the tolerance ϵ.

In this adaptive mesh approach, the spatial step size Δx is small in the region of the boundary layer, where a small Δt is needed. We could use a large Δt away from the boundary layer, where Δx is large. However, the time integration scheme requires that the time step must be equal for each grid point, unless an advanced local time stepping scheme is used. In the present work, we have used a second order accurate Crank-Nicolson method for both the advection and the viscous terms with a fractional

step projection method for the pressure gradient term. However, the time step, Δt, has also been adapted based on the CFL number. A maximum CFL number with the smallest Δx indicates how small a time step should be if an explicit method were used. Figure 4.6(b) shows the horizontal velocity through the vertical centre line of the cavity at $Re = 10^3$ for CFL = 1, 2, 3, 4 and 6. The time steps for corresponding CFL = 1, 2, 3, 4, 6 are presented in Table 4.2. These results confirm that a large CFL number or a large tolerance ϵ does not affect the solution significantly.

CFL	Time step (Δt)
1	6.24×10^{-3}
2	1.25×10^{-2}
3	2.00×10^{-2}
4	2.49×10^{-2}
6	3.72×10^{-2}

Table 4.2: Time step corresponding to the CFL number.

The boundary layer is also resolved despite a large CFL number being used. According to the boundary layer theory, the thickness of a laminar boundary layer is given by (e.g., Batchelor, 2000)

$$\delta \sim \frac{L}{\sqrt{Re}}. \tag{4.4}$$

Figure 4.7 shows that boundary layer width, δ, decreases with the increase of Reynolds number, Re, where the theoretical logarithmic slope is -0.5. In Figure 4.7, a line with a logarithmic slope -0.6 fits well with computed boundary's width. This means that the numerical result of our adaptive mesh model is in good agreement with the theoretical result.

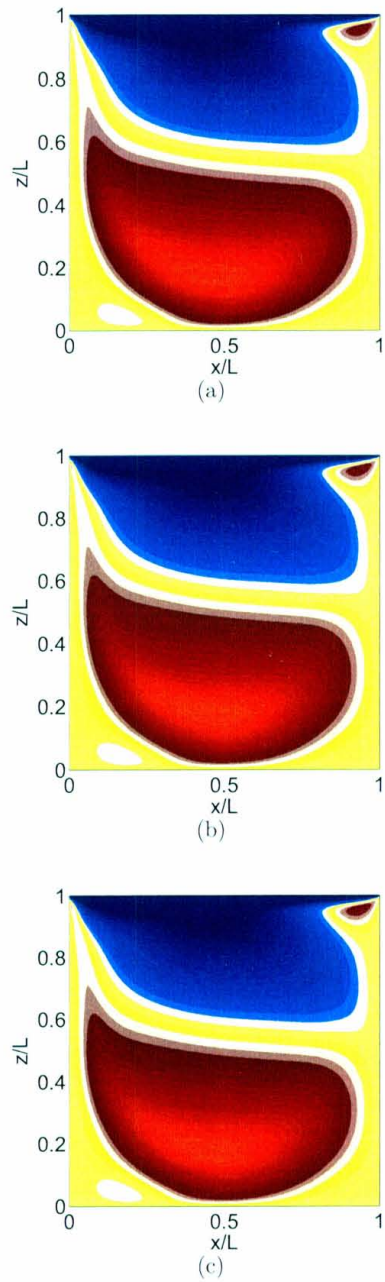

Figure 4.2: Horizontal velocity field (u) at (a) $t = 40$, (b) $t = 45$, (c) $t = 50$. The velocity does not change significantly if t is increased.

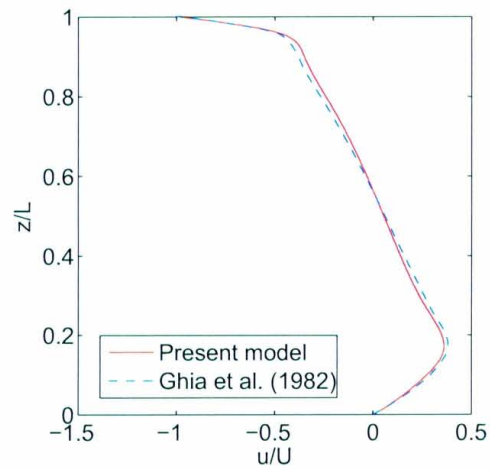

(a)

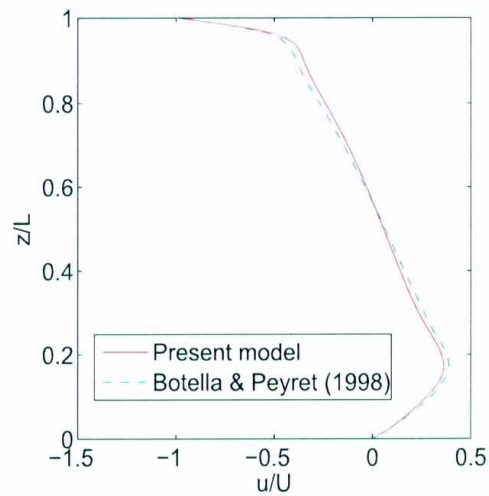

(b)

Figure 4.3: The horizontal velocity profile (u), along a vertical line at $x = 0.5$. (a) Comparison of the simulated results from the present model with the corresponding results adapted from Ghia *et al.* (1982), (b) Comparison of the simulated results from the present model with the corresponding results adapted from Botella & Peyret (1998).

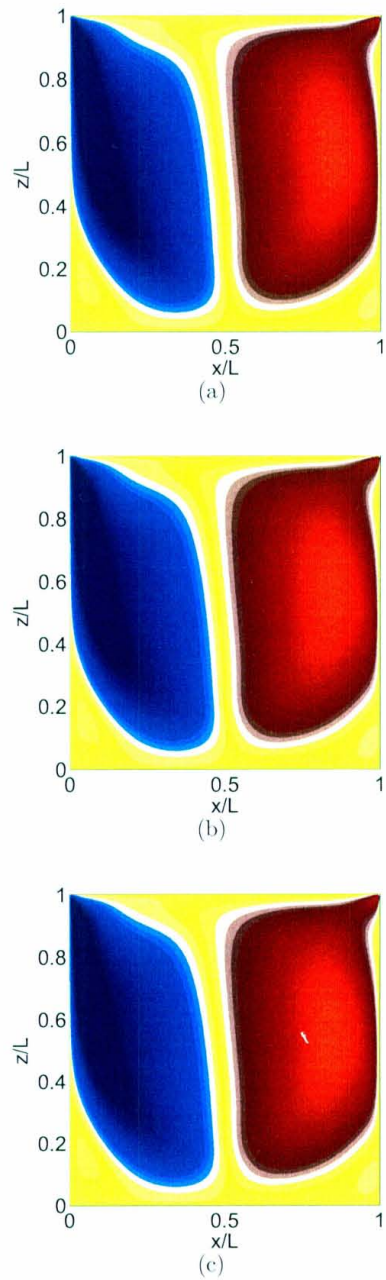

Figure 4.4: Vertical velocity field (w) at (a) $t = 40$, (b) $t = 45$, (c) $t = 50$. The velocity does not change significantly if t is increased.

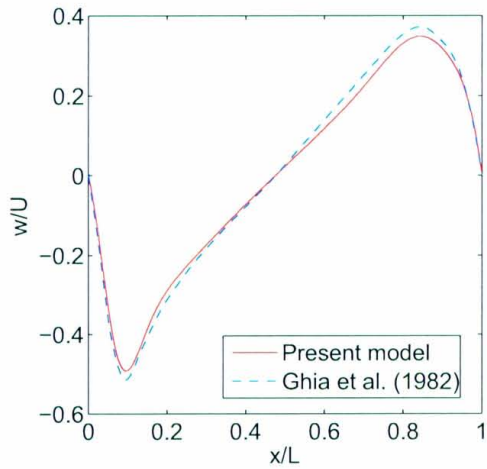

(a)

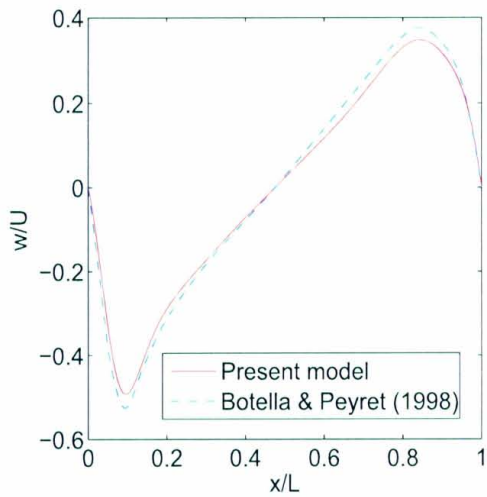

(b)

Figure 4.5: The vertical velocity profile (w), along a horizontal line at $z = 0.5$. (a) Comparison of the simulated results from the present model with the corresponding results adapted from Ghia *et al.* (1982), (b) Comparison of the simulated results from the present model with the corresponding results adapted from Botella & Peyret (1998).

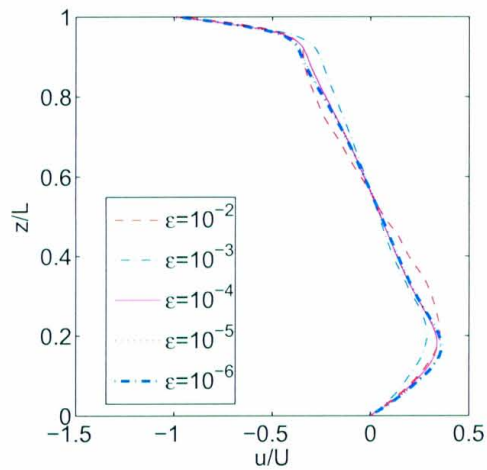

(a)

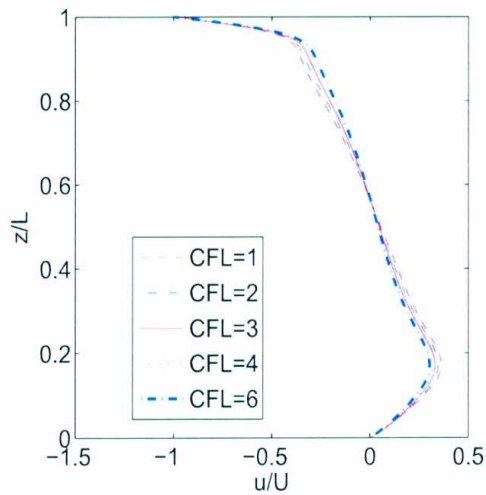

(b)

Figure 4.6: The horizontal velocity profile (u), along a vertical line at $x = 0.5$. (a) Spatial mesh adaptation results for the wavelet filter tolerance, $\epsilon = 10^{-2},\ 10^{-3},\ 10^{-4},\ 10^{-5},\ 10^{-6}$. Clearly we see that the error is controlled according to tolerance ϵ; (b) The time step adaptation for CFL $= 1,\ 2,\ 3,\ 4,\ 6$, where a large CFL indicates a large Δt. Note that an explicit scheme would require CFL ≤ 1. Using the large CFL value is a distinct feature of the present model.

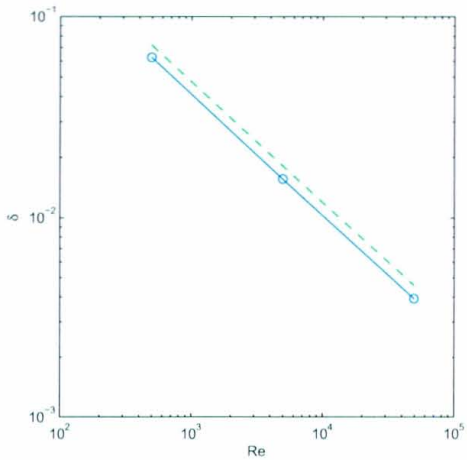

Figure 4.7: Boundary layer width(δ) as a function of Reynolds number(Re). A line with a slope of -0.6 fits well with the computed results.

4.2 Thermally driven flow

As a second test, consider another popular problem, the thermally driven square cavity flow that solves the Navier Stokes equation and energy equation for incompressible flows. De Vahl Davis & Jones (1983) organized a comparison exercise to calculate laminar natural convective flows in a square cavity up to Rayleigh number 10^6. About 30 groups participated in this exercise. Most of them used a finite difference method and confirmed the accuracy of benchmark solutions. As the boundary layer along the wall gets thinner, the flow becomes more difficult to calculate for large a Rayleigh number. Quere (1991) obtained the solutions of natural convection in a square 2-D differentially heated cavity with adiabatic top and bottom walls for values of Ra up to 10^8 using a pseudo-spectral Chebyshev algorithm. Mayne *et al.* (2000) provided the steady state and transient solution of thermally driven cavity flow by the h-adaptive finite element method for Reynolds number up to 10^8. From this comparison exper-

iment, we see that the numerical results are in good agreement with the reference solutions.

The dimensional form of the governing equations of the thermally driven cavity flow is similar to the form explained by Mayne *et al.* (2000) and the nondimensional form is very similar to the form explained by Quere (1991).

The equations of two dimensional thermally driven cavity flow can be derived from the three dimensional equations (2.22 - 2.26), using $\frac{\partial}{\partial y}(\cdot) = 0$, $v = 0$, $U = \sqrt{\frac{\kappa g \beta L \Delta\theta}{\nu}}$, $Ri = 1$ and $Fr = \infty$. Hence we get

$$\frac{\partial u}{\partial x} + \frac{\partial w}{\partial z} = 0, \tag{4.5}$$

$$\frac{\partial u}{\partial t} + u\frac{\partial u}{\partial x} + w\frac{\partial u}{\partial z} = -\frac{\partial p}{\partial x} + \frac{Pr}{\sqrt{Ra}}\left(\frac{\partial^2 u}{\partial x^2} + \frac{\partial^2 u}{\partial z^2}\right), \tag{4.6}$$

$$\frac{\partial w}{\partial t} + u\frac{\partial w}{\partial x} + w\frac{\partial w}{\partial z} = -\frac{\partial p}{\partial z} + \frac{Pr}{\sqrt{Ra}}\left(\frac{\partial^2 w}{\partial x^2} + \frac{\partial^2 w}{\partial z^2}\right) + Pr\ \theta, \tag{4.7}$$

$$\frac{\partial \theta}{\partial t} + u\frac{\partial \theta}{\partial x} + w\frac{\partial \theta}{\partial z} = \frac{1}{\sqrt{Ra}}\left(\frac{\partial^2 \theta}{\partial x^2} + \frac{\partial^2 \theta}{\partial z^2}\right), \tag{4.8}$$

where the non dimensional parameters are defined in Table 2.2. We will explain that this dimensionless form of governing equations helps us to compare our model with previously simulated benchmark results.

4.2.1 Geometry and boundary condition

The fluid is contained in a square domain, $\Omega = (0,1)\times(0,1)$, where $\partial\Omega$ is the boundary of Ω. Known flow conditions are used on all sides. Adiabatic boundary conditions are imposed on the top and bottom walls for the temperature, and the velocities at all boundaries are zero. The geometry and boundary conditions are shown in Figure 4.8. Initially the fluid inside the cavity is at rest.The boundary conditions are:

$$u = w = 0 \text{ on the boundary } \partial\Omega \text{ of } \Omega.$$

$$\theta = 0.5 \text{ on } x = 0 \text{ and } \theta = -0.5 \text{ on } x = 1,\ 0 \leq z \leq 1.$$

$$\frac{\partial \theta}{\partial z} = 0 \text{ on } z = 0 \text{ and } z = 1,\ 0 \leq x \leq 1.$$

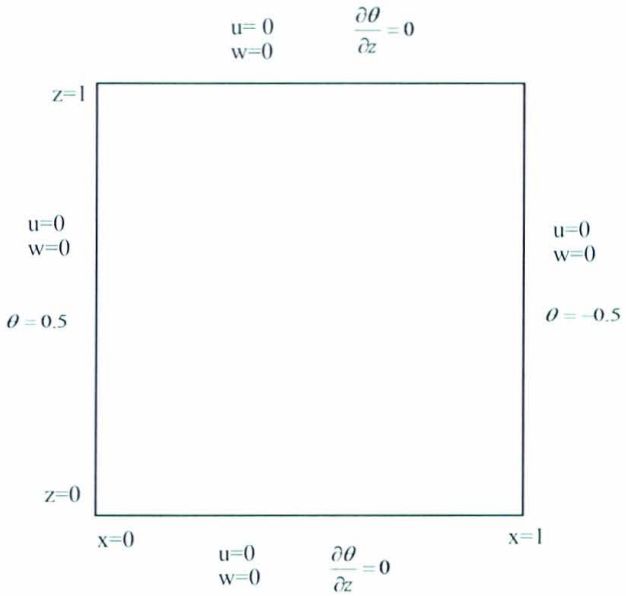

Figure 4.8: Thermally driven cavity flow configuration, coordinates, and boundary conditions.

The proposed fully implicit adaptive mesh method has been applied to simulate the thermally driven cavity flow in order to test the numerical accuracy and the effectiveness of the model.

4.2.2 Reference numerical model

The numerical model described by Quere (1991) is considered as the reference model. The governing equations of this reference model are also given by the equations (4.5 -4.8). The boundary conditions and the problem geometry of the reference model

is the same as discussed in section 4.2.1. We have also considered the dimensional equations from Mayne *et al.* (2000) for numerical conversion.

4.2.3 Numerical results

4.2.3.1 Dependence on the Rayleigh number, Ra

The time dependent equations (4.5-4.8) have been solved using the proposed method. In order to study the effect of the Rayleigh number on the flow, we have conducted simulations for $10^3 \leq Ra \leq 10^9$, and $Pr = 0.71$. These simulations help us to compare the model's performance with those results that were also presented in Mayne *et al.* (2000). For the comparison with the reference results we have presented the results for $10^3 \leq Ra \leq 10^8$. The temperature distributions (θ), for $10^3 \leq Ra \leq 10^9$ are shown in Figure 4.9 using colour contours. We observed that the temperature fields have reached steady states which are strongly dependent on Ra in the way that the large Ra have been delayed to reach the steady state. The temperature profile, $\theta(x, 0.5)$, along a horizontal line at $z = 0.5$, near the boundary for $10^3 \leq Ra \leq 10^8$ is presented in Figure 4.11(a). From Figure 4.11(a), we observe that if Ra increases, the horizontal gradient of θ decreases. The corresponding reference results adapted from Mayne *et al.* (2000) are also presented in Figure 4.11(b). From the comparison, we observe that the result is in good agreement with the reference result.

Let us present the vertical velocity fields for $10^3 \leq Ra \leq 10^8$ in Figure 4.10. The vertical velocity profiles, $w(x, 0.5)$, along a horizontal line at $z = 0.5$, near the boundary, are shown in Figure 4.11(c) and the corresponding reference results are presented in Figure 4.11(d). From Figures 4.11(c) and 4.11(d), we observe that for large Ra the maxima increases. Despite a slight disagreement at high Ra, that is associated with the scales U and L, and also considering that the flow tends to

a turbulent regime at $Ra \geq 10^8$, present results are in good agreement with the reference results.

The horizontal velocity fields for $10^3 \leq Ra \leq 10^8$ are presented in Figure 4.12. From this Figure, we observe that if Ra increases, the strongest velocity occurs near the top ($z = 1$) and bottom ($z = 0$) boundaries. Such a velocity distribution is also consistent with the temperature distribution that is shown in Figure 4.9. We see that the development of the thermal boundary layer is a result of convective circulation. From Figure 4.12, we observe that the horizontal velocity depends on Ra as well. The adapted meshes for $10^3 \leq Ra \leq 10^8$ are presented in Figure 4.13. These meshes show the distribution of grid points for calculating of the solution presented in Figure 4.9. From Figure 4.13, we observe that large Ra requires more grid points and that grid points are concentrated near the boundaries.

4.3 Summary

In this Chapter we have presented the performance of the proposed adaptive mesh model for simulating two types of flows. First, we study the numerical simulation of a shear driven flow. Second, we simulate a thermally driven flow. These two flows are commonly used for testing new CFD algorithms. From the comparison, it is apparent that the adaptive mesh simulation of lid driven cavity flow is in good agreement with the data presented in Ghia *et al.* (1982) and Botella & Peyret (1998). The adaptive multilevel simulation of the thermally driven flow in a cavity shows a good agreement with that of Mayne *et al.* (2000) and Quere (1991) and the references therein.

In the next chapter we will present numerical simulation of a heat island flow and study the effect of the dimensionless parameter.

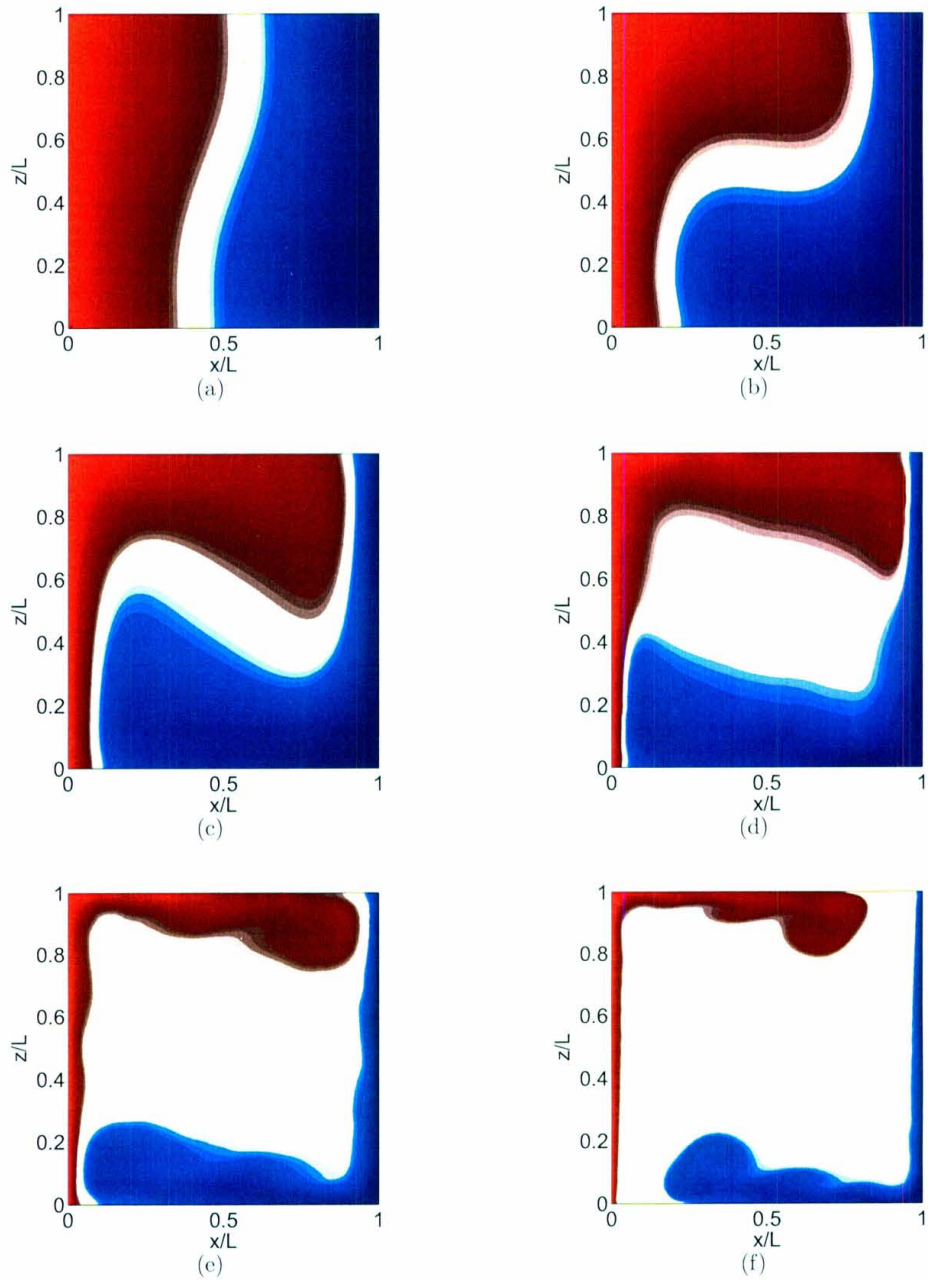

Figure 4.9: Temperature field (θ) for different Rayleigh numbers. (a) $Ra = 10^3$, (b) $Ra = 10^4$, (c) $Ra = 10^5$, (d) $Ra = 10^6$, (e) $Ra = 10^7$, (f) $Ra = 10^8$.

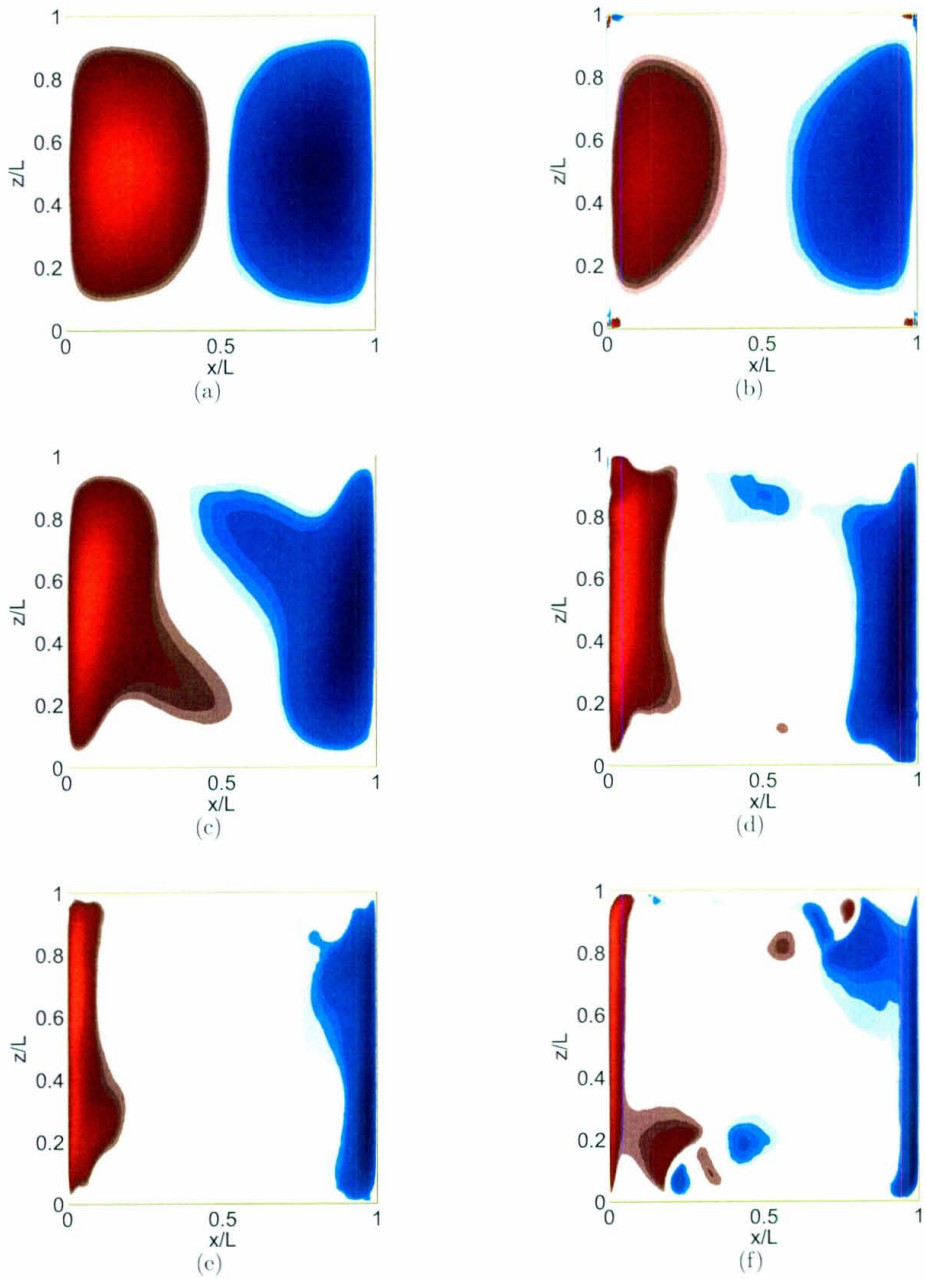

Figure 4.10: Vertical velocity field (w) for different Rayleigh numbers. (a) $Ra = 10^3$, (b) $Ra = 10^4$, (c) $Ra = 10^5$, (d) $Ra = 10^6$, (e) $Ra = 10^7$, (f) $Ra = 10^8$.

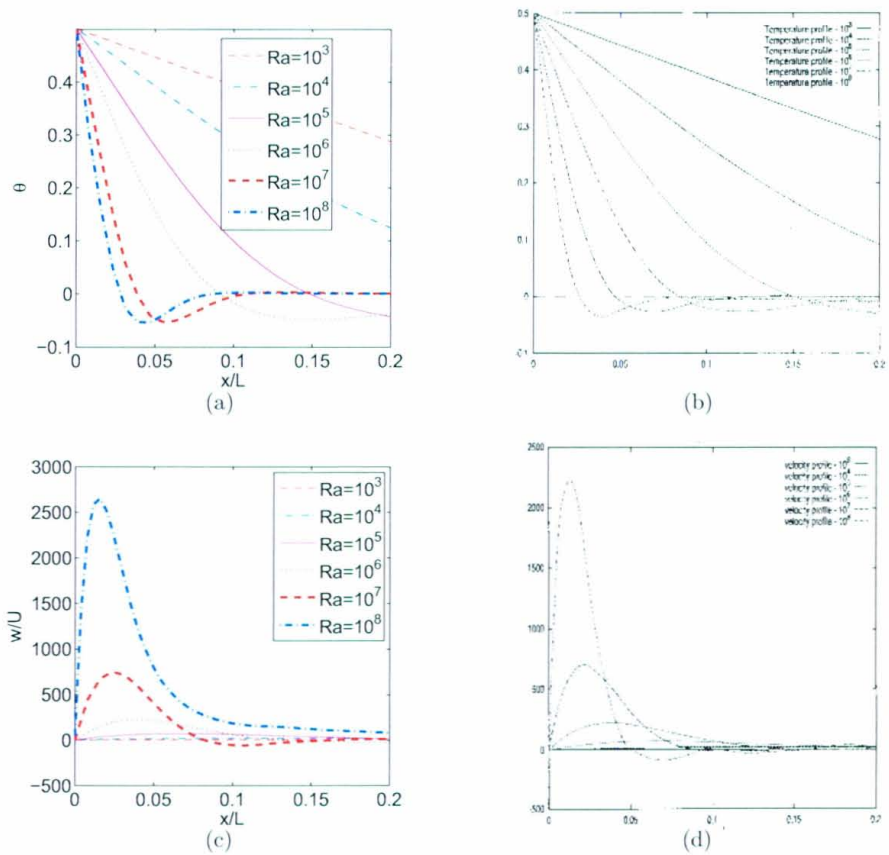

Figure 4.11: (a) Temperature profile, θ on z/L = 0.5 near boundary, (b) Temperature profile, θ on z/L = 0.5 near boundary adapted from Mayne *et al.* (2000), (c) Vertical velocity profile, w/U on z/L = 0.5 near boundary, (d) Vertical velocity profile, w/U on z/L = 0.5 near boundary adapted from Mayne *et al.* (2000).

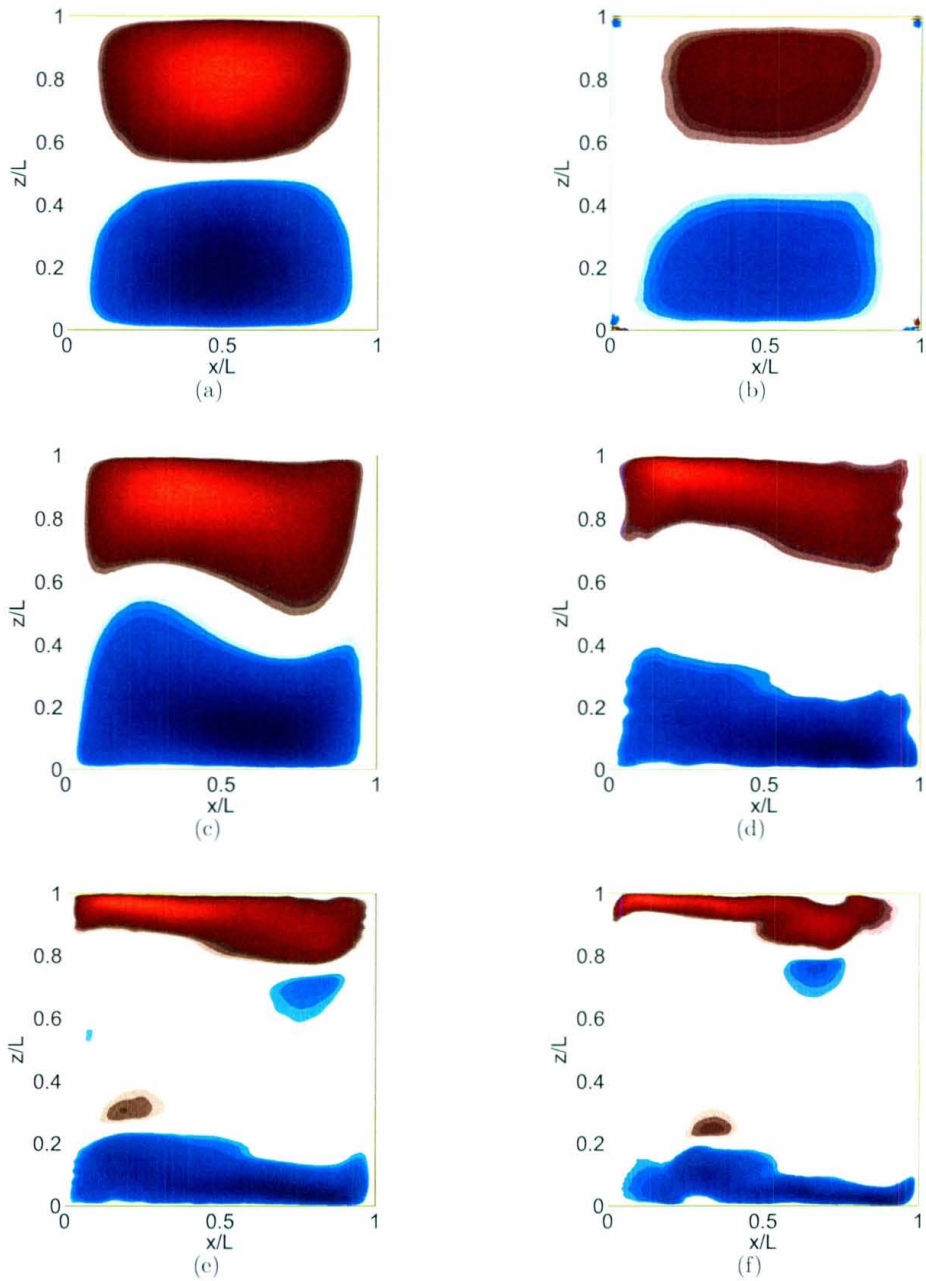

Figure 4.12: Horizontal velocity field (u) for different Rayleigh numbers. (a) $Ra = 10^3$, (b) $Ra = 10^4$, (c) $Ra = 10^5$, (d) $Ra = 10^6$, (e) $Ra = 10^7$, (f) $Ra = 10^8$.

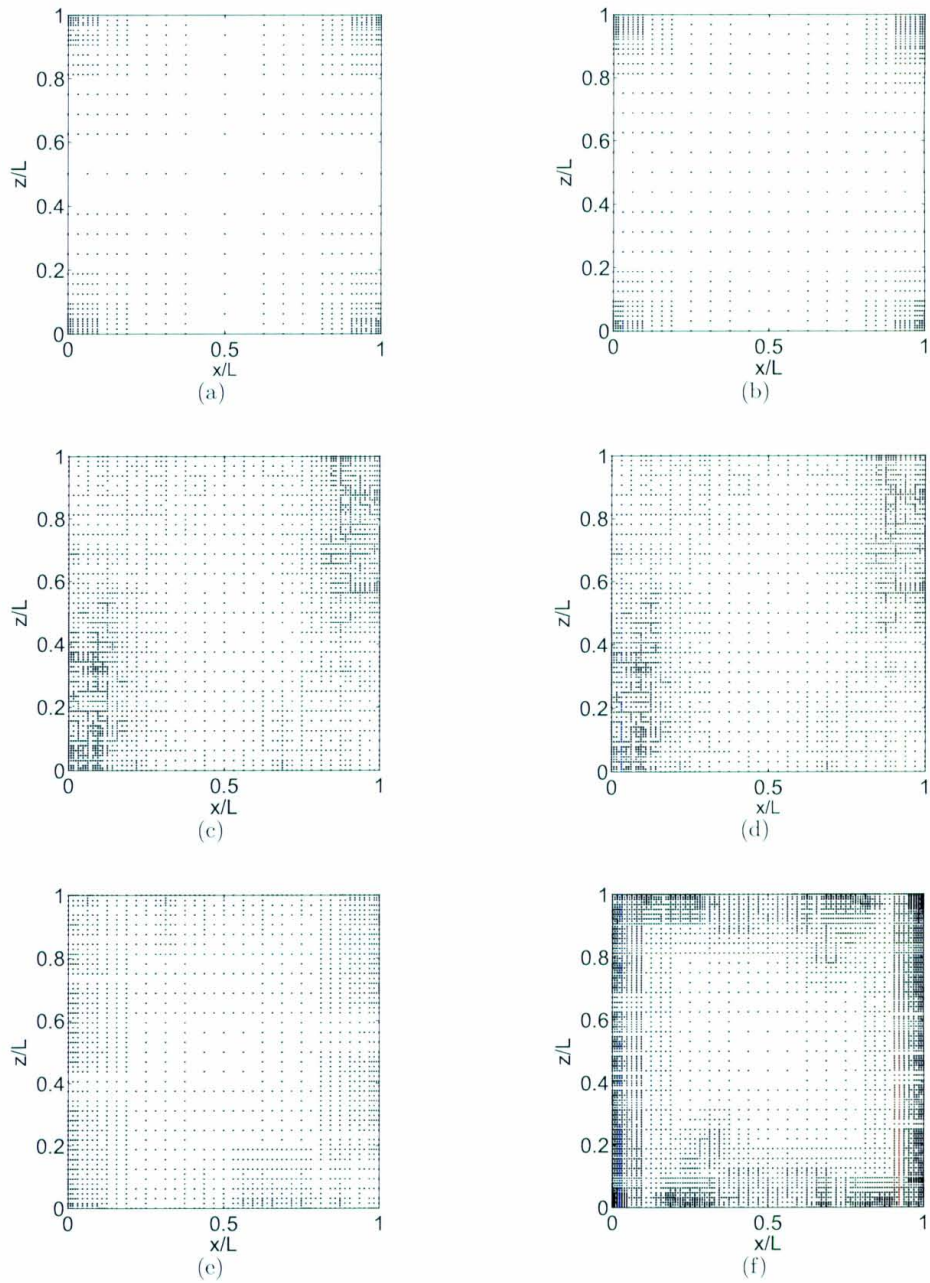

Figure 4.13: Adapted grid. (a) $Ra = 10^3$, (b) $Ra = 10^4$, (c) $Ra = 10^5$, (d) $Ra = 10^6$, (e) $Ra = 10^7$, (f) $Ra = 10^8$.

Chapter 5

Numerical Simulation of Heat Island Circulation

This chapter presents the numerical simulation of an idealized heat island circulation, where the effects of the earth's rotation are neglected. The governing equations for representing a stably stratified dry atmosphere are obtained from the dimensionless equations (2.22 - 2.26), using $\frac{\partial}{\partial y}(\cdot) = 0$ and $v = 0$ for further simplification so that we can simulate circulation in a vertical plane.

5.1 Governing equations

Similar to the mathematical model presented in Niino *et al.* (2006) as well as in Dubois & Touzani (2009), we obtain the following set of PDEs.

$$\frac{\partial u}{\partial x} + \frac{\partial w}{\partial z} = 0, \tag{5.1}$$

$$\frac{\partial u}{\partial t} + u\frac{\partial u}{\partial x} + w\frac{\partial u}{\partial z} = -\frac{\partial p}{\partial x} + \sqrt{\frac{Pr}{Ra}}\left(\frac{\partial^2 u}{\partial x^2} + \frac{\partial^2 u}{\partial z^2}\right), \tag{5.2}$$

$$\frac{\partial w}{\partial t} + u\frac{\partial w}{\partial x} + w\frac{\partial w}{\partial z} = -\frac{\partial p}{\partial z} + \sqrt{\frac{Pr}{Ra}}\left(\frac{\partial^2 w}{\partial x^2} + \frac{\partial^2 w}{\partial z^2}\right) + Ri\ \theta, \tag{5.3}$$

$$\frac{\partial \theta}{\partial t} + u\frac{\partial \theta}{\partial x} + w\frac{\partial \theta}{\partial z} + \frac{1}{Ri(Fr)^2}w = \frac{1}{\sqrt{RaPr}}\left(\frac{\partial^2 \theta}{\partial x^2} + \frac{\partial^2 \theta}{\partial z^2}\right), \tag{5.4}$$

where the dimensionless parameters are given by Table 2.2. This model is governed by the four nondimensional parameters Ra, Ri, Pr and Fr. Using a fixed Prandtl number (*e.g.* $Pr = 1$ in Lu *et al.* (1997); Niino *et al.* (2006) and $Pr = 0.71$ in Dubois & Touzani (2009)), the flow regime is determined by the nonlinear parameters Ra, Ri and Fr. We will discuss how the circulation is affected if these parameters vary.

5.2 Geometry and boundary condition

Choosing the most appropriate boundary conditions for such a simplified model of heat island circulation remains challenging. As described in Niino *et al.* (2006), a heat island fluid flow is a typical horizontal convection as a result of heating in the vertical direction, so the computational domain needs to be very large or unbounded in the horizontal direction, *e.g.* see the discussion in Dubois & Touzani (2009).

The computational domain of the present simulation extends non-dimensional intervals $\left[-\frac{X}{2}, \frac{X}{2}\right]$ and $[0, Z]$ in the horizontal and vertical directions respectively; *i.e.*, $\Omega = \left(-\frac{X}{2}, \frac{X}{2}\right) \times (0, Z)$ and $\partial\Omega$ is the boundary of Ω. A characteristic length scale $L = 1$ km, which is the width of the heat island, is used to make the domain dimensionless. Hence, the horizontal extent of the domain is $X = 10$ km and the vertical extent is $Z = 1$ km unless otherwise stated. The computational domain is presented in Figure 5.1, where the horizontal extent, L, of the localized heat source is also shown. This domain is wide compared with its height.

The unbounded propagation in the horizontal circulation can be modelled either using a periodic boundary condition or using a Neumann boundary condition in the

horizontal direction, *i.e.* on lateral boundaries. In the vertical direction, the velocity components satisfy $u = w = 0$ at $z = 0$ and $z = 1$, and the temperature satisfies $\theta = 0$ at $z = 1$ (e.g. Niino *et al.*, 2006). At $z = 0$, an isolated surface heating is introduced by

$$\theta(x, z = 0, t) = \theta_0(x)$$

with

$$\theta_0(x) = \frac{1}{2}\left(\tanh\left(\frac{2x+1}{2\zeta}\right) - \tanh\left(\frac{2x-1}{2\zeta}\right)\right), \tag{5.5}$$

where $\zeta = 2.5 \times 10^{-2}$. In Dubois & Touzani (2009), the velocity boundary conditions are no-slip, *i.e.* $u = w = 0$ on all boundaries. In Niino *et al.* (2006), the velocity boundary conditions are free-slip, *i.e.* $u = 0$, $\frac{\partial w}{\partial x} = 0$ on $x = \pm X/2$, and $\frac{\partial u}{\partial z} = 0$, $w = 0$ on $z = 0$ and $z = 1$. We have found that the no-slip velocity conditions on all four boundaries along with $\theta(\pm\frac{X}{2}, z) = 0$ introduce numerical artifacts for the temperature profile on both lateral boundaries.

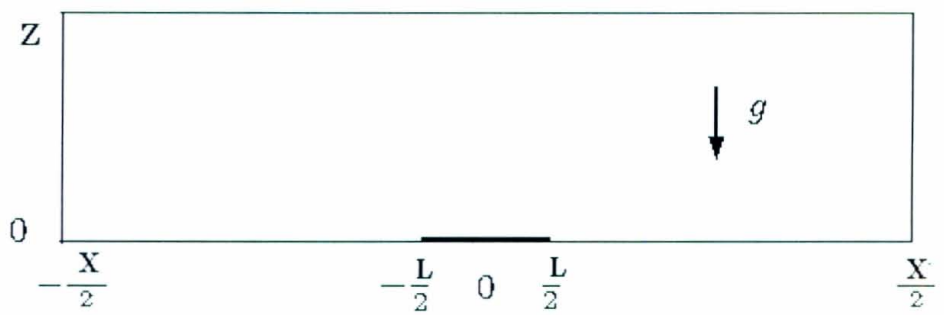

Figure 5.1: Computational domain and surface heating source of heat island circulation.

Numerical simulations have been compared with the results obtained from Dubois & Touzani (2009), providing quantitative estimates on the model's performance for

$Ra = 10^3$, 10^4, and 10^5. Our results also have a good agreement with those from Niino *et al.* (2006) despite that different governing equations and boundary conditions were used.

5.2.1 Comparison with reference model

In Dubois & Touzani (2009), a numerical model for heat island circulation was presented where a filter function was used to modify the convective terms in the heat equation, which was parametrized by γ. If $\gamma = 0$, then the governing equations of Dubois & Touzani (2009) are the same as those presented in (5.1)-(5.4). This filter function acts like an artificial sponge layer near the lateral boundaries, where the convective temperature has been damped through the outflow. From this paper, we have compared the temperature profiles $\theta(x, 0.5, T)$, $\theta(0, z, T)$ and velocity profiles $w(x, 0.5, T)$, $w(0, z, T)$, which serve as the quantitative verification of our simulations.

The governing equations of Niino *et al.* (2006) are the same as those used in this thesis except that Niino *et al.* (2006) used the buoyancy equation to replace the temperature equation. Using different scaling parameters, Niino *et al.* (2006) provided a mathematical analysis, explaining various flow regimes. These regimes are in agreement with what we have found from our simulations.

5.3 Numerical results

5.3.1 Dependence on Rayleigh number, Ra

In order to study how a heat island circulation is affected by varying Rayleigh numbers, we have conducted simulations for $10^3 \leq Ra \leq 10^8$, $Pr = 0.71$ $Ri = 1$, and $Fr = 1$. These simulations exhibit flow regimes with increasing Ra, as well as help us

to compare the model's performance with those results that were presented in Dubois & Touzani (2009) for $10^3 \leq Ra \leq 10^5$.

First, we have observed that the flow has a strong dependence on Ra in the way that a quasi steady state of θ is reached as early as $t \leq 15$ for $Ra = 10^3$. This has been delayed with an increase of Ra, where θ reaches a steady state at $t \leq 30$ for $Ra = 10^4$ and $t \leq 60$ for $Ra = 10^5$. Moreover, the flow does not reach a steady state for $Ra \geq 10^6$. Since the governing equations, boundary conditions, and parameters, *e.g.* $10^3 \leq Ra \leq 10^5$, for this simulation are equal or equivalent with those of Dubois & Touzani (2009), a comparison ensures a cross checking for the present model's performance. These temperature distributions are shown in Figure 5.2 using colour contours. The temperature profiles, $\theta(x, 0.5, 60)$, along a horizontal line at $z = 0.5$, for $10^3 \leq Ra \leq 10^5$ are presented in Figure 5.3(a). From Figure 5.3(a), we observe that if Ra increases, the horizontal gradient of θ along the line $z = 0.5$ increases. The corresponding reference result adapted from Dubois & Touzani (2009) is shown in Figure 5.3(b). There is a slight disagreement near the boundary. This is mainly due to the smaller computational domain of the present model compared to that of the reference model. Note that the reference model used a filter function for damping out the solution artificially near the boundary. Despite a little dissimilarity near the boundary, present results are in good agreement with the reference results.

Again, the temperature profiles, $\theta(0, z, 60)$, along a vertical line at $x = 0$, for $10^3 \leq Ra \leq 10^5$ are presented in Figure 5.3(c), and the corresponding reference results are presented in Figure 5.3(d). From the comparison, we observe that the vertical gradient of θ decreases for large Ra. The temperature profiles along a vertical line through the centre of the cavity have a good agreement with the reference results.

Let us consider the vertical velocity fields for $10^3 \leq Ra \leq 10^8$, which are presented in Figure 5.4. The vertical velocity profiles, $w(x, 0.5, 60)$ along a horizontal line at

$z = 0.5$ for $10^3 \leq Ra \leq 10^5$ are shown in Figure 5.5(a), and the corresponding reference results are in Figure 5.5(b). From the comparison, we observe that for large Ra the maxima that occur near $x = 0$ is also high for both cases. Again the comparison for the vertical velocity profile $w(0, z, 60)$ along a vertical line at $x = 0$ is presented in Figures 5.5(c) and 5.5(d). From the comparison we observe that the largest Ra provides a maximum vertical velocity near the point $(0, 0.5)$, and such a maximum decreases if Ra increases. This comparison shows a good agreement with the reference result. The temperature and vertical velocity profiles along a horizontal line at $z = 0.5$, for $10^3 \leq Ra \leq 10^8$ are presented in Figure 5.6. From Figure 5.6(a), we observe that for large Ra the temperature maximum decreases and the temperature profile becomes oscillatory. Figure 5.6(b) shows that for large Ra the vertical velocity also becomes oscillatory.

Kimura (1975) found an interesting feature of heat island circulation from laboratory and numerical studies. Kimura (1975) observed from experiments that heat island circulation has two types of flow regimes. One has a single maximum of updraft at the centre of the heat island, which is called type C, and the other has two maxima of updraft at both edges of the heat island, which is called type E. When the differential heating is strong, a strong narrow updraft is contentrated above the centre of the island; on the other hand, when the differential heating is weak, the centre of the circulation is located at the edges of the heat island. Niino *et al.* (2006) also observed that nonlinear heat island circulation has two different types of flow regimes, and the transition between the two regimes is determined by a nondimensional parameter (for details see Niino *et al.*, 2006). From our simulation we also observe that the flow regimes are characterized by the nondimensional parameter Ra; type C flow occurs for $Ra \leq 10^5$ and type E occurs for $Ra \geq 10^6$. Figure 5.7 shows two different types of flow regimes for $Ra = 10^3$, and $Ra = 10^6$. From our simulations,

we observe clearly that the results are in good qualitative agreement with the results provided by Kimura (1975) and Niino *et al.* (2006).

The horizontal velocity, (u), and vorticity, (ω), are shown for $Ra = 10^3, 10^4, 10^5, 10^6, 10^7, 10^8$, $Pr = 0.71$, $Ri = 1$, and $Fr = 1$ in Figures 5.8, and 5.9. We observe from Figures 5.8 and 5.9 that the horizontal velocity, (u), and the vorticity, (ω) are strongly dependant on Ra. The adapted grid for these simulations is presented in Figure 5.10. The number of grid points used by these simulations is shown in Table 5.1. From this Table we observe that for large Ra the number of grid points increases, as the flow becomes oscillatory for large Ra.

Ra	Grid points
10^3	5662
10^4	7812
10^5	9665
10^6	25349
10^7	47496
10^8	72187

Table 5.1: Number of grid points corresponding to Ra.

5.3.2 Dependence on Richardson number, Ri

The Richardson number, Ri, is the most important dimensionless parameter for thermally driven flows, which is defined by $Ri = \frac{\Delta\theta L_c}{\theta_0 U^2} g$. For thermally driven flows, Ri measures the importance of natural convection compared to forced convection. Ri also indicates the relation between the Grashof number, Gr and the Reynolds number, Re. Commonly the Richardson number is also defined as $Ri = \frac{Gr}{Re^2}$. The natural

convection is negligible for $Ri < 0.1$, forced convection is negligible for $Ri > 10$, and neither is negligible for $0.1 < Ri < 10$. However, if $Ri = 1$, then the circulation is a buoyancy driven flow. Figure 5.12, shows the temperature profiles for $Ra = 10^6$, $Ri = 3, 5, 10$, $Pr = 0.71$ and $Fr = 1$. From this Figure, we can easily realize how the temperature field has been affected by Ri. From Figure 5.12, we see clearly that if the Richardson number increases, the fluid above the heat island warms up, and hence rises upward due to the decrease of density with the increase of temperature (*e.g.* large $\Delta\theta$).

5.3.3 Dependence on Froude number, Fr

The dimensionless parameter Froude number, Fr, is defined by $Fr = \frac{U}{L\sqrt{\frac{g}{\theta_0}\frac{\partial\bar{\theta}}{\partial z}}}$. The Froude number measures relative importance between inertia and gravitational force. Fr also indicates the relative significance between characteristic velocity and gravitational wave velocity. Commonly, the Froude number is also defined as $Fr = \frac{U}{LN}$, where the buoyancy frequency is given by $N^2 = \frac{g}{\theta}\frac{\partial\bar{\theta}}{\partial z}$. Hence, we can explain the effect of Fr if gravitational force is important, such as large scale flows in the atmosphere or in the ocean. In the present work, we have conducted simulations of buoyancy driven flow at $Ri = 1$ for various values of Fr in order to understand how abruptly a circulation is affected if Fr is changed. Figure 5.11 presents the temperature distribution for $Ra = 10^6$, $Fr = 0.25, 20, 1000, \infty$, $Pr = 0.71$, and $Ri = 1$. From this Figure, we can easily realize how the temperature field has been affected with Fr. Note here that if the surface is heated, the fluid above warms up, and hence rises upward due to the decrease of density with the increase of temperature. When $Fr < \infty$, we have $\frac{\partial\bar{\theta}}{\partial z} > 0$, and the flow is stably stratified. When $Fr = \infty$, we have $\frac{\partial\bar{\theta}}{\partial z} = 0$, and the flow is neutrally stable. The stability of the atmosphere is explained in Kundu & Cohen

(2008). In the stable atmosphere, if an air parcel is lifted adiabatically, the parcel would tend to return to its original position because of the buoyancy frequency, N. Since $N > 0$ for $Fr < \infty$ and $N = 0$ for $Fr = \infty$, we see the rising of the hot plume above the heated island has been reduced.

5.4 Summary

In this chapter, the adaptive mesh simulations of heat island circulation have been presented for $10^3 \leq Ra \leq 10^8$. From the simulations, we observe that the flow has a strong dependence on the nondimensional parameters Ra, Ri, and Fr. From the comparison, we also observe that the adaptive mesh simulations of heat island circulations are in good agreement with those in Kimura (1975), Niino *et al.* (2006) and Dubois & Touzani (2009). From Table 5.1, we observe that for large Ra the number of grid points increases, as the flow becomes oscillatory for large Ra. The simulations have been conducted with resolution 1024×128 and 2048×256; however, from Table 5.1, we observe that only a fraction of the grid points from a prescribed resolution is required for actual calculation. Figure 5.13 shows the relationship between number of grid points and corresponding required CPU time used by these simulations. From Figure 5.13, we observe clearly that CPU time for these simulations increases linearly with an increase in the number of grid points.

In the next chapter we will discuss potential benefits of the proposed model, and future research direction, where this model may be useful.

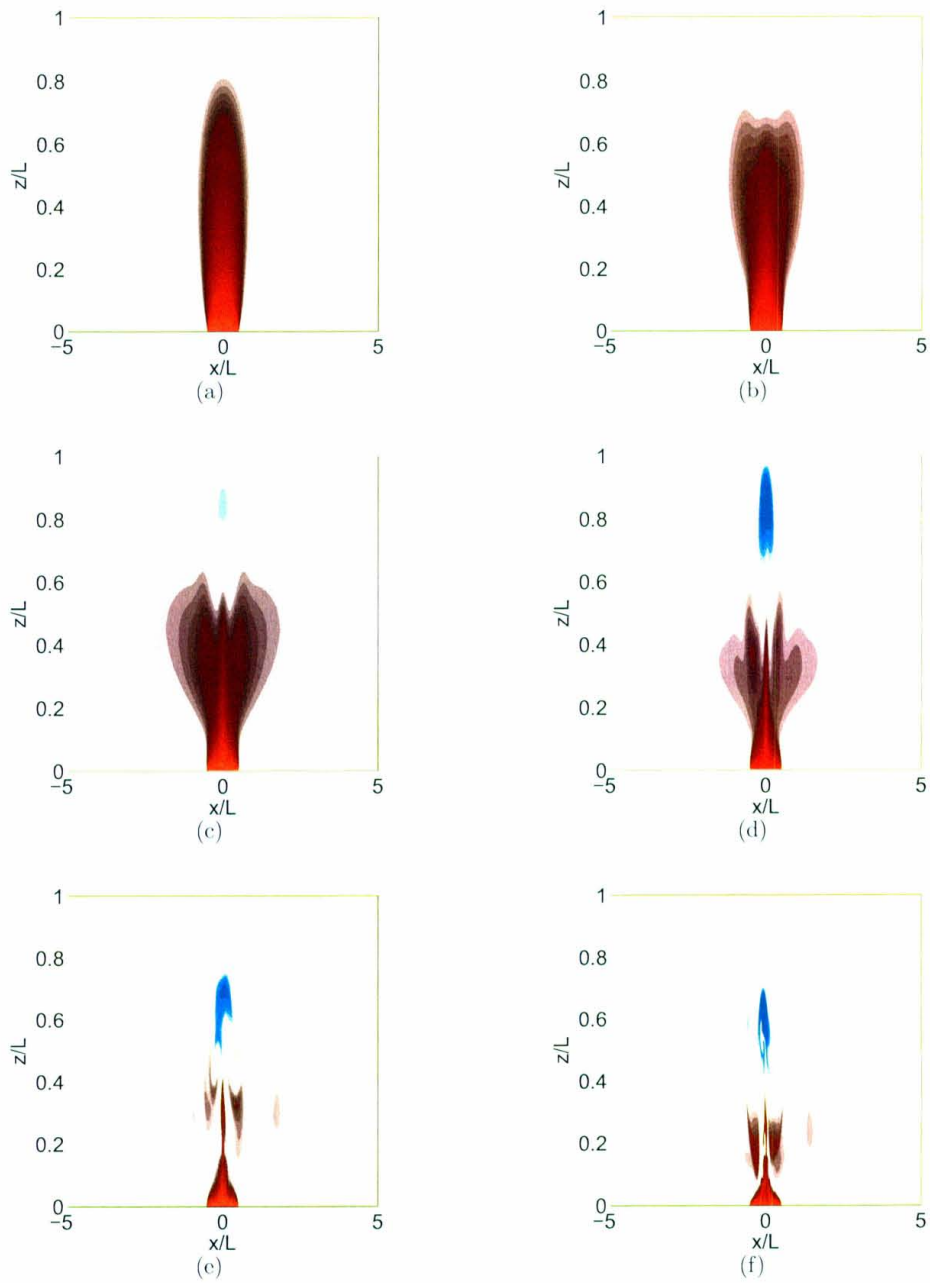

Figure 5.2: Temperature field (θ) for $Ri = 1$, $Fr = 1$, and $Pr = 0.71$. (a) $Ra = 10^3$, (b) $Ra = 10^4$, (c) $Ra = 10^5$, (d) $Ra = 10^6$, (e) $Ra = 10^7$, (f) $Ra = 10^8$.

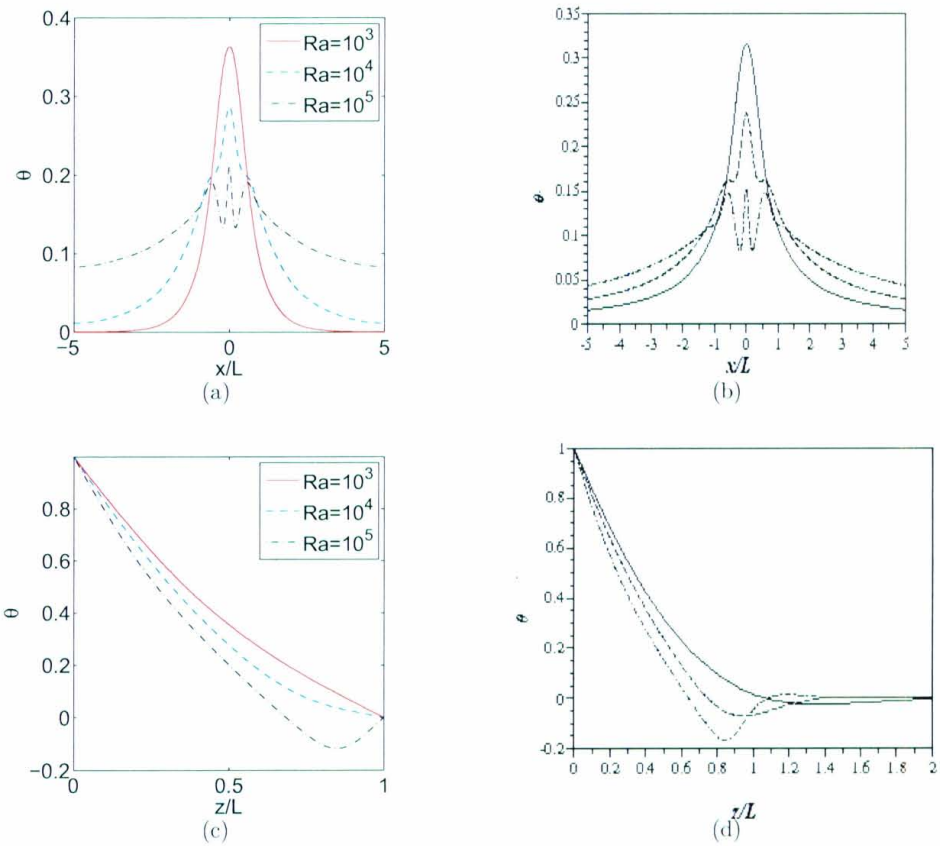

Figure 5.3: (a) Temperature field (θ) at the centre of the vertical line z/L=0.5, (b) Temperature profile (θ) at the centre of the vertical line z/L=0.5 (adapted from Dubois & Touzani, 2009), (c) Temperature profile (θ) at the centre of the horizontal line x/L=0, (d) Temperature profile (θ) at the centre of the horizontal line x/L=0 (adapted from Dubois & Touzani, 2009).

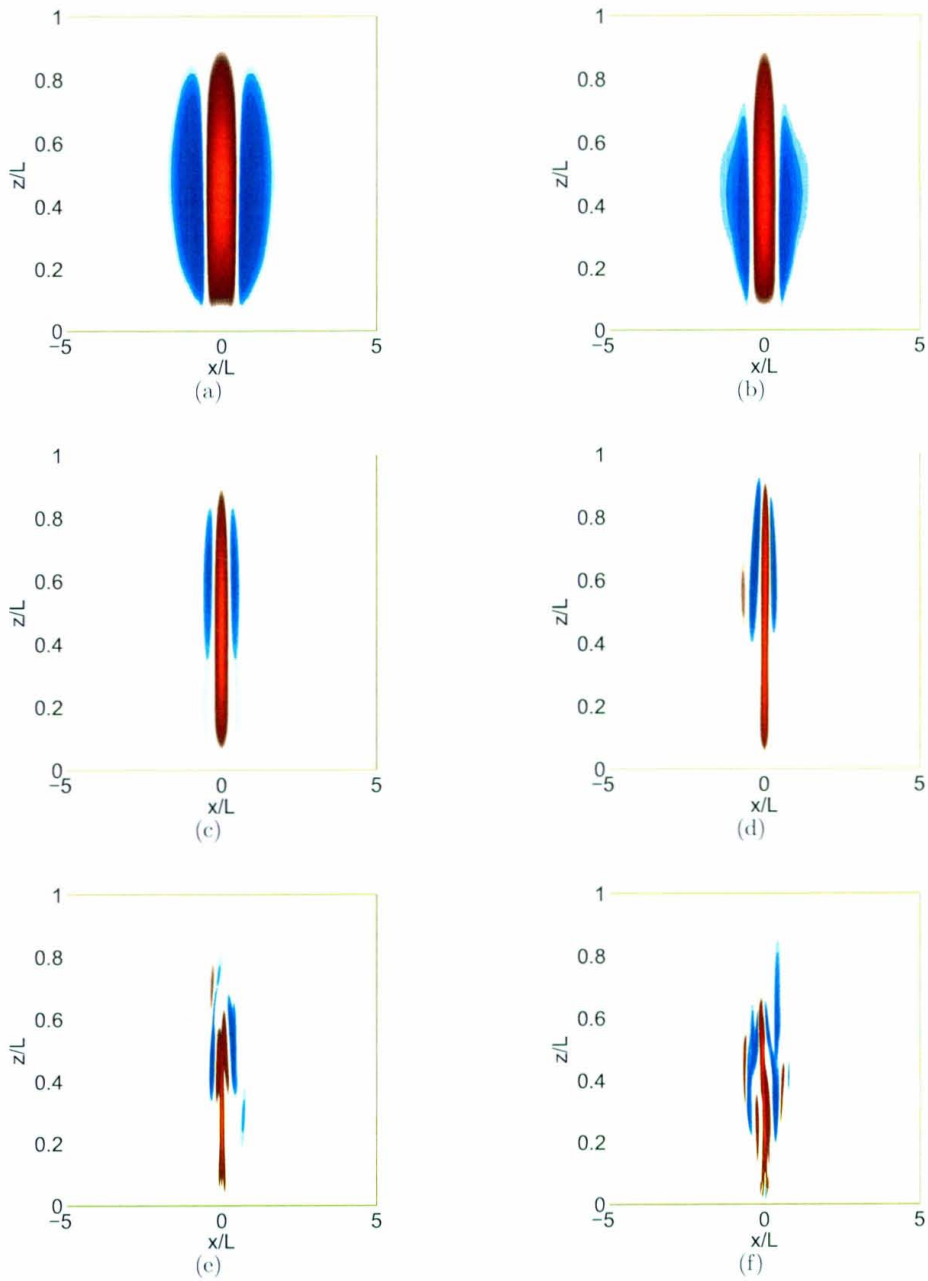

Figure 5.4: Vertical velocity filed (w) for $Ri = 1$, $Fr = 1$, and $Pr = 0.71$. (a) $Ra = 10^3$, (b) $Ra = 10^4$, (c) $Ra = 10^5$, (d) $Ra = 10^6$, (e) $Ra = 10^7$, (f) $Ra = 10^8$.

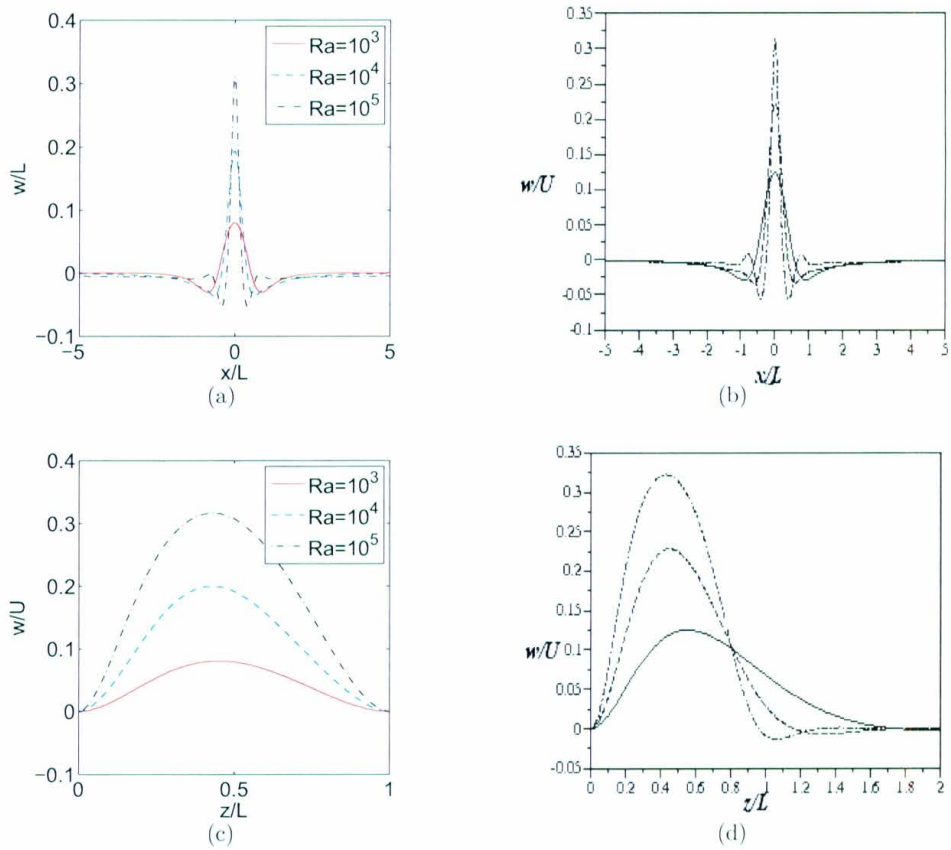

Figure 5.5: (a) Vertical velocity profile (w) at the centre of the vertical line z/L=0.5, (b) Vertical velocity profile (w) at the centre of the vertical line z/L=0.5 (adapted from Dubois & Touzani, 2009), (c) Vertical velocity profile (w) at the centre of the horizontal line x/L=0, (d) Vertical velocity profile (w) at the centre of the horizontal line x/L=0 (adapted from Dubois & Touzani, 2009).

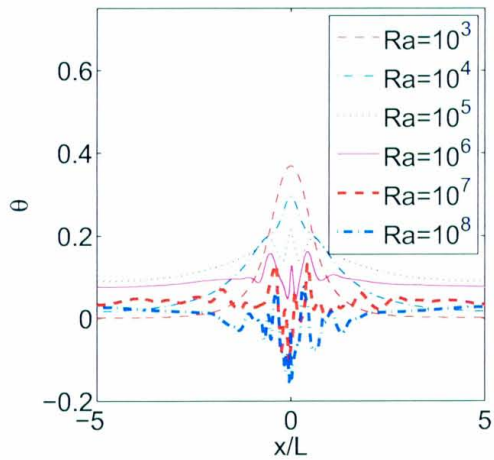

(a)

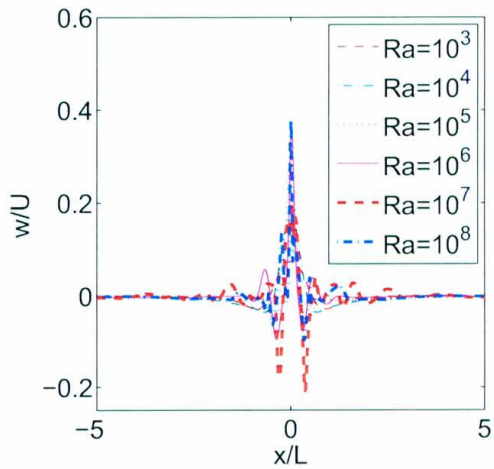

(b)

Figure 5.6: (a) Temperature profile, (θ), for $10^3 \leq Ra \leq 10^8$ $Ri = 1$, $Fr = 1$, and $Pr = 0.71$ at the centre of the vertical line z/L=0.5, (b) Vertical velocity profile, (w), for $10^3 \leq Ra \leq 10^8$ $Ri = 1$, $Fr = 1$, and $Pr = 0.71$ at the centre of the vertical line z/L=0.5.

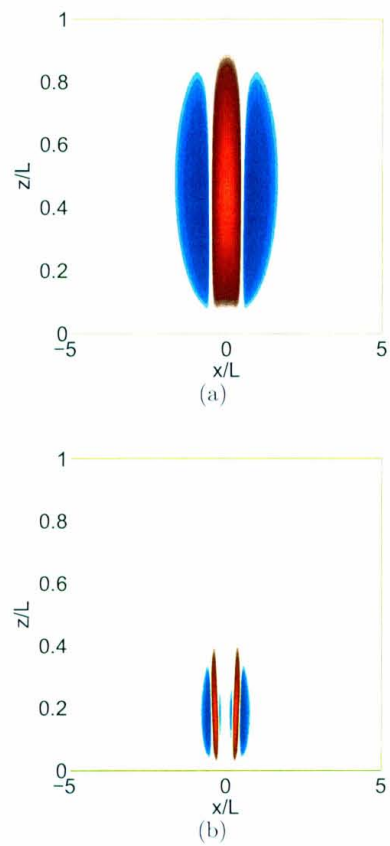

Figure 5.7: Vertical velocity field (w) for $Fr = 1$, $Ri = 1$, and $Pr = 0.71$. (a) $Ra = 10^3$, (b) $Ra = 10^6$.

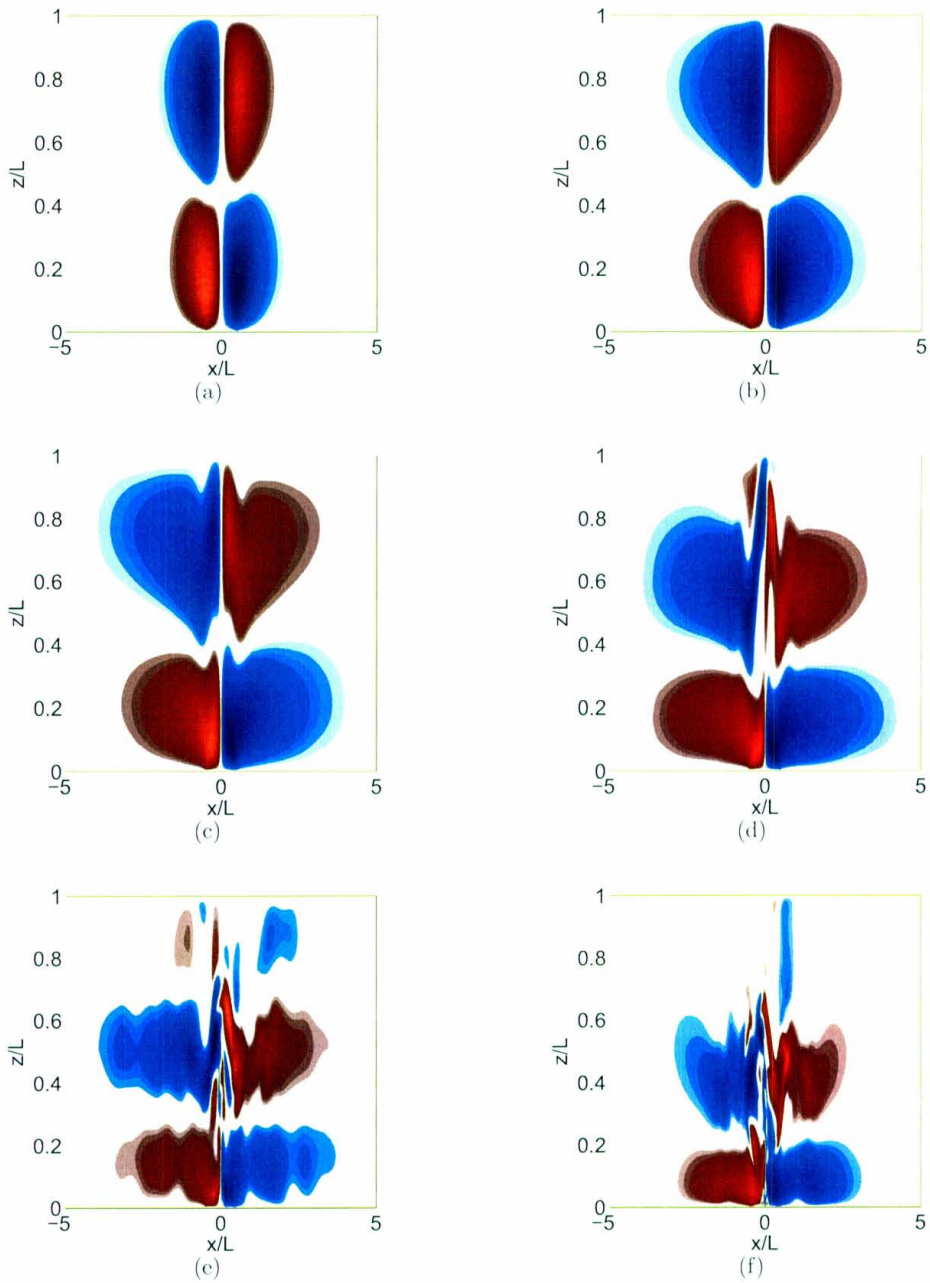

Figure 5.8: Horizontal velocity field (u) for $Ri = 1$, $Fr = 1$, and $Pr = 0.71$. (a) $Ra = 10^3$, (b) $Ra = 10^4$, (c) $Ra = 10^5$, (d) $Ra = 10^6$, (e) $Ra = 10^7$, (f) $Ra = 10^8$.

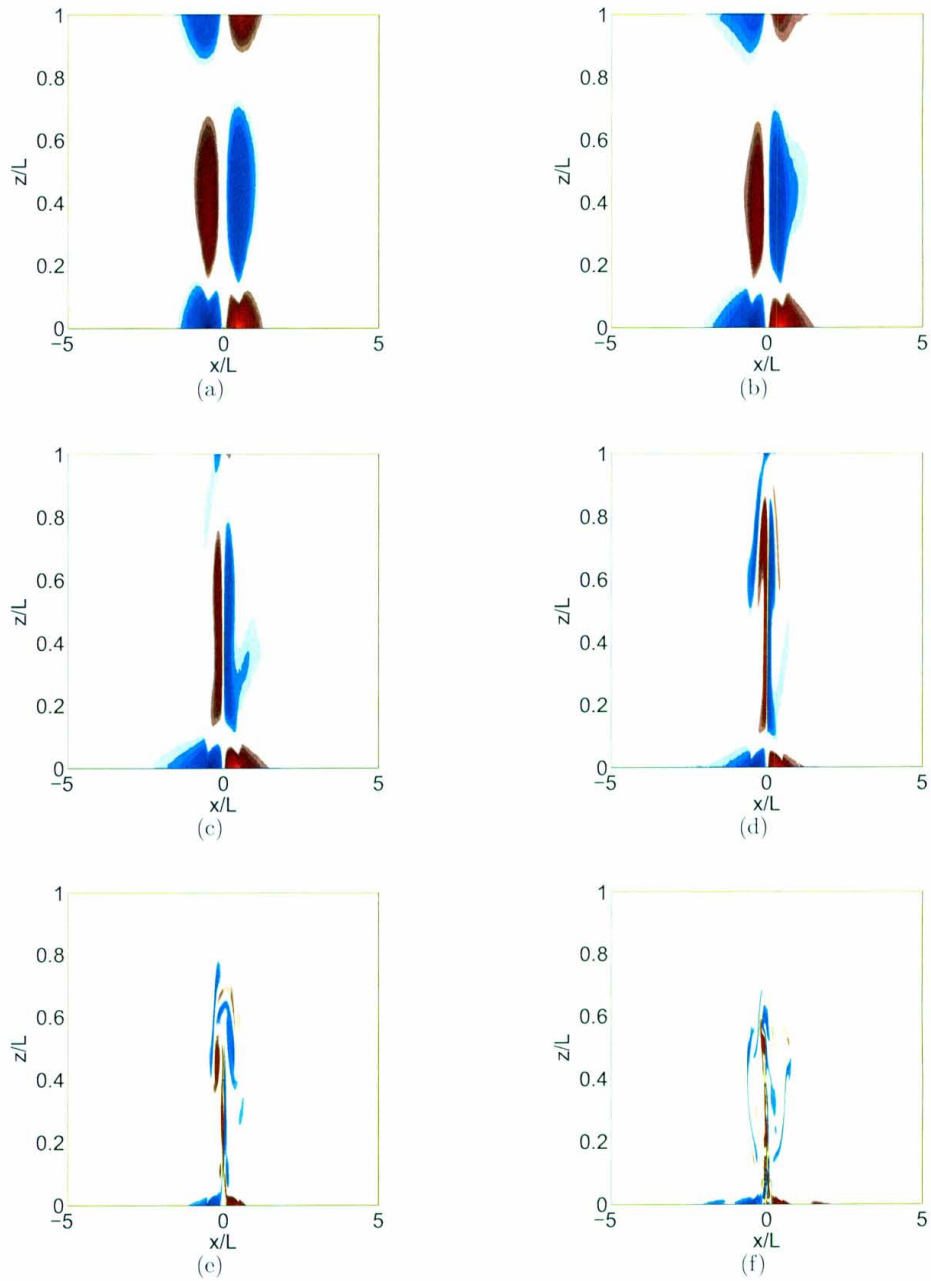

Figure 5.9: Vorticity field (ω) for $Ri = 1$, $Fr = 1$, and $Pr = 0.71$. (a) $Ra = 10^3$, (b) $Ra = 10^4$, (c) $Ra = 10^5$, (d) $Ra = 10^6$, (e) $Ra = 10^7$, (f) $Ra = 10^8$.

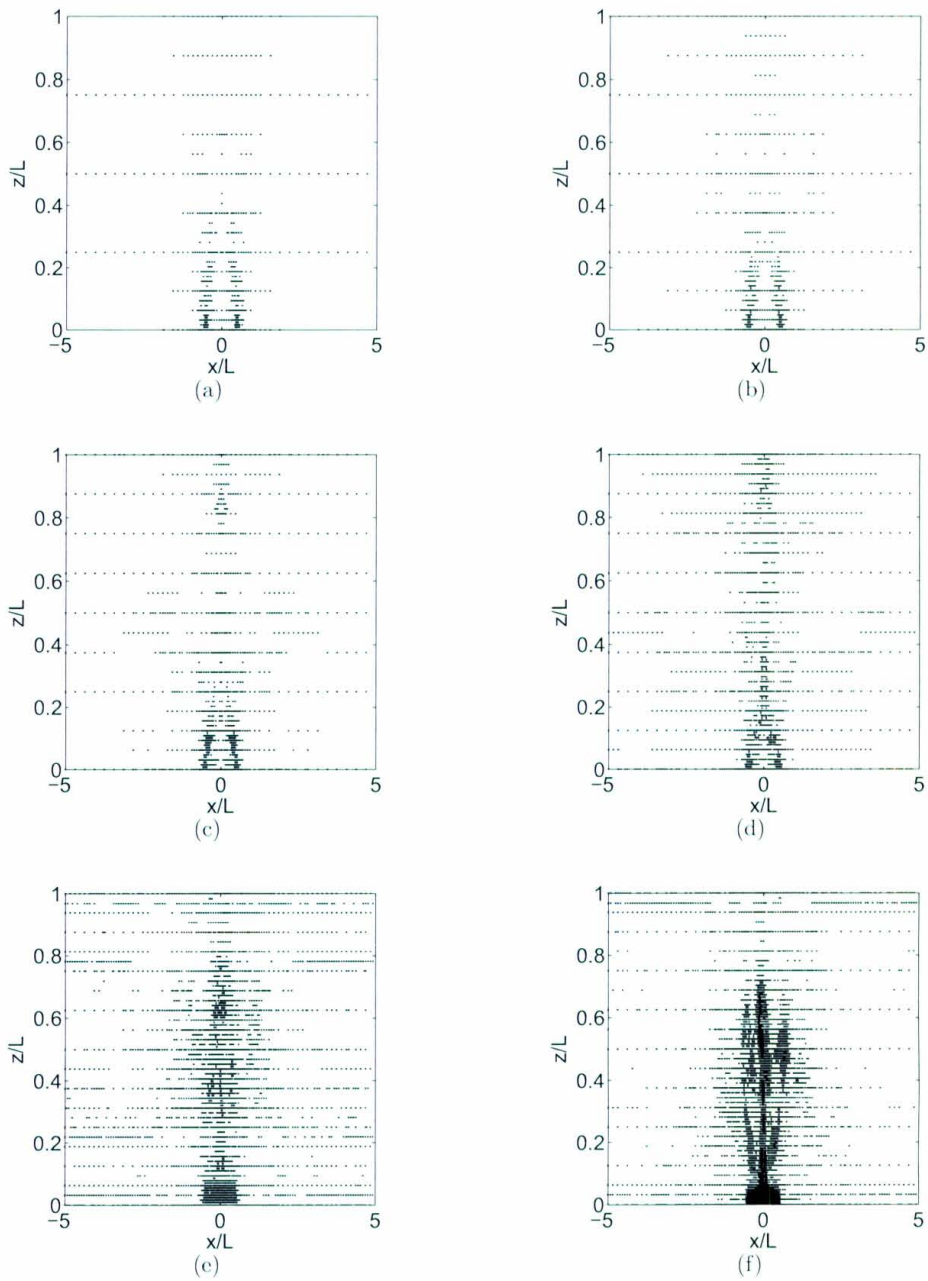

Figure 5.10: Adapted grid for $Ri = 1$, $Fr = 1$ and $Pr = 0.71$. (a) $Ra = 10^3$, (b) $Ra = 10^4$, (c) $Ra = 10^5$, (d) $Ra = 10^6$, (e) $Ra = 10^7$, (f) $Ra = 10^8$.

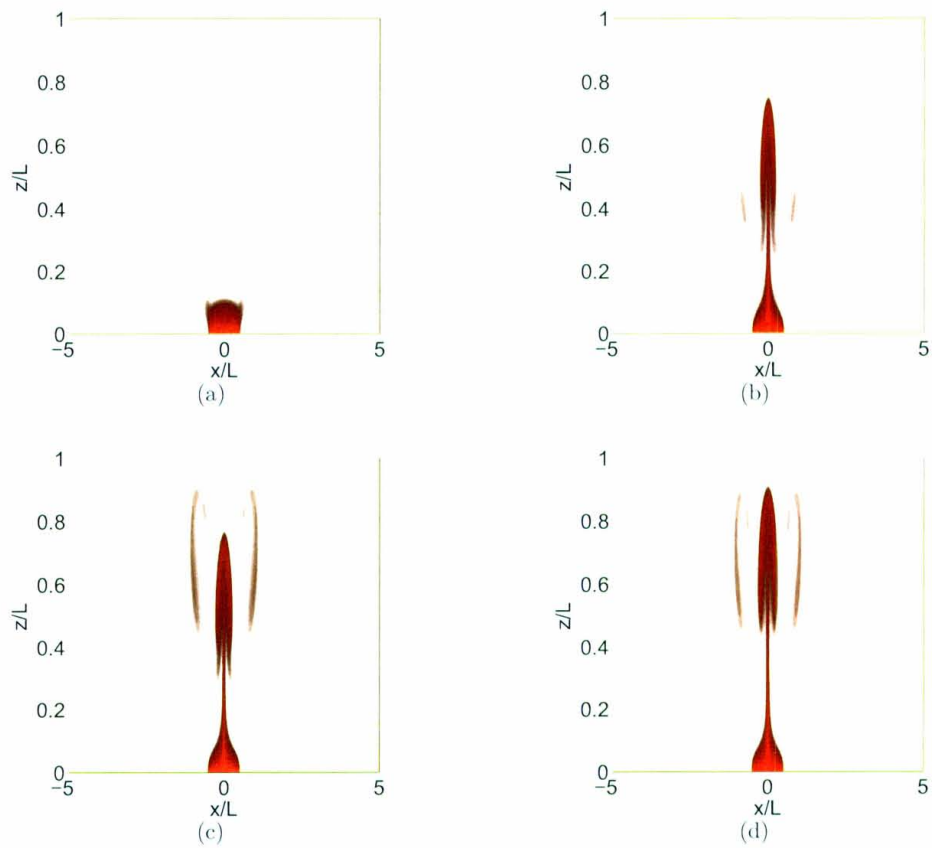

Figure 5.11: Effect of Froude number on temperature field (θ) for $Ra = 10^6$, $Ri = 1$ and $Pr = 0.71$. (a) $Fr = 0.25$, (b) $Fr = 20$, (c) $Fr = 1000$, (d) $Fr = \infty$.

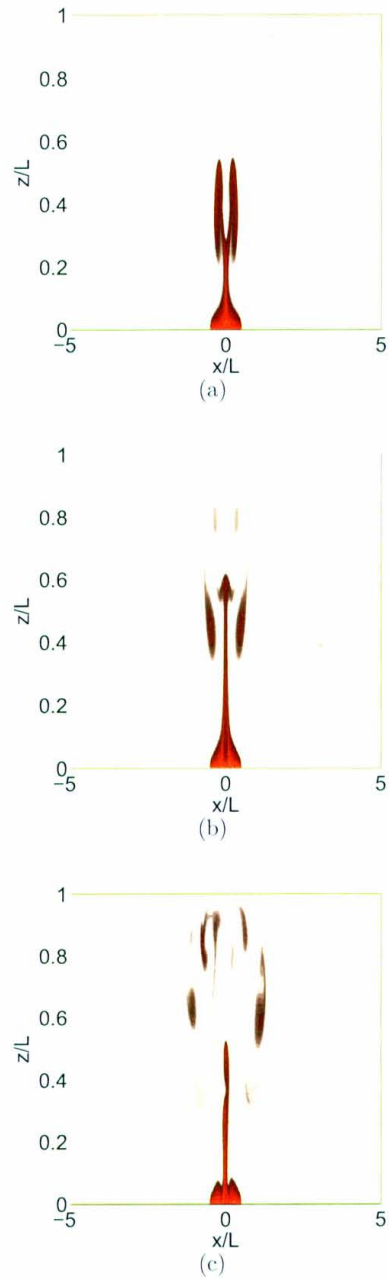

Figure 5.12: Effect of Richardson number on temperature field (θ) for $Ra = 10^6$, $Fr = 1$ and $Pr = 0.71$. (a) $Ri = 3$, (b) $Ri = 5$, (c) $Ri = 10$.

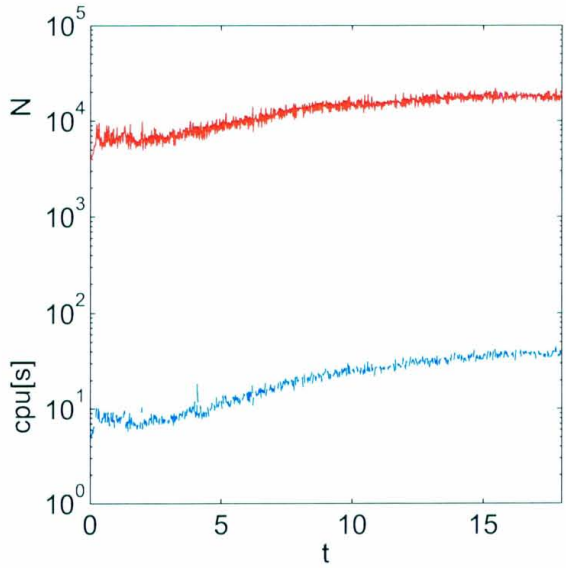

Figure 5.13: The elapsed CPU time[s] at each time step and the number of adapted grid points, N is plotted as a function of simulation time, t. A visual inspection between these two curves indicates that CPU time[s] has a linear relationship with the number of grid points, N.

Chapter 6

Conclusion and Future Research Direction

In the last chapter of this thesis, we summarize its main contribution, and briefly outline future research direction.

6.1 Conclusion

We have analyzed and derived the governing equations for thermally driven flows, and proposed an adaptive mesh method for simulating thermally driven flows. We have verified our proposed model with two of the most popular test cases, (i) lid driven cavity flow and (ii) thermally driven cavity flow, since these flows are commonly used for verification of CFD codes.

The lid driven cavity flow has been simulated for $Re = 1000$ and resolution, $N^2 = 160^2$. Note that in the present work, only a fraction of the grid points from the prescribed resolution is required for the actual simulation. For example, only $3,416$ grid points out of 160^2 grid points are significant for this simulation with $\epsilon = 10^{-3}$,

which is about 5.2% compared to the grid points used in Ghia *et al.* (1982), and about 13.34% compared to what was used in Botella & Peyret (1998). The simulation of the lid-driven cavity is also conducted for large tolerance ϵ and large CFL. These results confirm that a large ϵ or a large CFL does not affect the solution significantly. We have also conducted the thermally driven flows in a cavity for $10^3 \leq Ra \leq 10^9$ and for a different resolution, $N^2 = 128^2,\ 256^2$. We observe that large Ra requires a large number of grid points, which is also a fraction of the prescribed resolution and concentrated near the boundary.

Heat island flow circulation has been conducted for $10^3 \leq Ra \leq 10^8$ and resolution $1024 \times 128, 2048 \times 256$. However, the adaptive mesh simulations of heat island circulation require only a fraction of the grid points from a prescribed resolution for the actual simulation. From the comparison, we observe that the adaptive mesh simulations of heat island circulations are in good agreement with those of Kimura (1975), Niino *et al.* (2006) and Dubois & Touzani (2009). We also observe that the required CPU time for these simulations of heat island circulations increases linearly with an increase in the number of grid points. Hence adaptivity saves CPU time as the model is $\mathcal{O}(\mathcal{N})$.

6.2 Future developments

The present two dimensional time dependent thermally driven flow in a heat island simulation using an adaptive mesh method has the ability of resolving localized dynamics, so the extension of the present work for three dimensional simulations is a next step. This present work can also be explored in the field of atmospheric science; for example, the verification of the CFD model with observation would provide further enlighten to research in the field of atmospheric modelling. Such a model would

play an important role in predicting local weather in fast growing urban areas.

Bibliography

Alam, J. M. 2011 Towards a multiscale approach for computational atmospheric modelling. *Monthly Weather Review* .

Alam, J. M. & Lin, J. C. 2008 Toward a fully lagrangian atmospheric modeling system. *Monthly Weather Review* **136**, 4653 – 4667.

Baik, J.-J. & Chun, H.-Y. 1997 A dynamical model for urban heat islands. *Boundary-Layer Meteorology* **83**, 463–477, 10.1023/A:1000346229951.

Baik, J.-J., Kim, Y.-H. & Chun, H.-Y. 2001 Dry and Moist Convection Forced by an Urban Heat Island. *Journal of Applied Meteorology* **40**, 1462–1475.

Barrett, R., Berry, M., Chan, T. F., Demmel, J., Donato, J. M., Dongara, J., Eijkhout, V., Pozo, R., Romine, C. & der Vorst, H. V. 2002 *Templetes for the solution of linear system: building block for iterative method*, 2nd edn. society for industrial and applied mathematics.

Batchelor, G. 2000 *An introduction to fluid dynamics*. Cambridge University Press.

Bejan, A. & Kraus, A. D. 2003 *Heat transfer handbook*, , vol. 1, chap. 7, pp. 525–571. John Willey & Sons Inc.

Botella, O. & Peyret, R. 1998 Benchmark spectral results on the lid-driven cavity flow. *Computers & Fluids* **27** (4), 421 – 433.

Bruneau, C.-H. & Saad, M. 2006 The 2d lid-driven cavity problem revisited. *Computers & Fluids* **35** (3), 326 – 348.

Chorin, A. J. 1968 Numerical solution of the navier-stokes equations. *Mathematics of Computation* **22** (104), pp. 745–762.

De Vahl Davis, G. & Jones, I. P. 1983 Natural convection in a square cavity: A comparison exercise. *International Journal for Numerical Methods in Fluids* **3** (3), 227–248.

Delage, Y. & Taylor, P. A. 1970 Numerical studies of heat island circulations. *Boundary-Layer Meteorology* **1**, 201–226, 10.1007/BF00185740.

Dubois, T. & Touzani, R. 2009 A numerical study of heat island flows: Stationary solutions. *International Journal for Numerical Methods in Fluids* **59** (6), 631–655.

E, W. & Liu, J.-G. 1995 Projection method i: Convergence and numerical boundary layers. *SIAM Journal on Numerical Analysis* **32** (4), pp. 1017–1057.

Ghia, U., Ghia, K. N. & Shin, C. T. 1982 High-re solutions for incompressible flow using the navier-stokes equations and a multigrid method. *Journal of Computational Physics* **48** (3), 387 – 411.

Han, J. & Baik, J. 2008 A Theoretical and Numerical Study of Urban Heat Island Induced Circulation and Convection. *Journal of Atmospheric Sciences* **65**, 1859 1877.

HARLOW, F. H. & WELCH, J. E. 1965 Numerical calculation of time-dependent viscous incompressible flow of fluid with free surface. *Physics of Fluids* **8** (12), 2182 – 2189.

IPSEN, I. C. & MEYER, C. D. 1998 The idea behind krylov methods. *American Mathematical Monthly* **105** (10), 889–899.

JABLONOWSKI, C. 2004 Adaptive grids in weather and climate modeling. PhD thesis, University of Michigan.

JABLONOWSKI, C., HERZOG, M., PENNER, J. E., OEHMKE, R. C., F., S. Q. & VAN LEER, B. 2004 Adaptive grids for weather and climate models. pp. 233–250. ECMWF Seminar Proceedings on Recent Developments in Numerical Methods for Atmospheric and Ocean Modelling, UK.

JONES, J. E. & WOODWARD, C. S. 2000 Newton-krylov-multigrid solvers for large-scale, highly heterogeneous, variably saturated flow problems.

KELLY, C. 1995 *Iterative method for linear and nonlinear equations*. Society of industrial and applied mathematics.

KIM, Y.-H. & BAIK, J.-J. 2002 Maximum Urban Heat Island Intensity in Seoul. *Journal of Applied Meteorology* **41**, 651–659.

KIMURA, R. 1975 Dynamics of steady convections over heat and cool islands. *Journal of the Meteorological Society of Japan* **53** (6), 440–457.

KUNDU, P. K. & COHEN, I. M. 2008 *Fluid Mechanics*, 4th edn. Academic Press.

LEVEQUE, R. J. 2007 *Finite difference methods for ordinary and partial differential equations: steady-state and time-dependent problems*. Society for industrial and applied mathematics.

Lin, Y.-L. 2007 *MESOSCALE DYNAMICS*. Cambridge University Press.

Lu, J., Pal Arya, S., Snyder, W. H. & Lawson, Jr., R. E. 1997 A Laboratory Study of the Urban Heat Island in a Calm and Stably Stratified Environment. Part I: Temperature Field. *Journal of Applied Meteorology* **36**, 1377–1391.

Martin, C. L. & Pielke, R. A. 1983 The Adequacy of the Hydrostatic Assumption in Sea Breeze Modeling over Flat Terrain. *Journal of Atmospheric Sciences* **40**, 1472–1481.

Mayne, D. A., Usmani, A. S. & Crapper, M. 2000 h-adaptive finite element solution of high rayleigh number thermally driven cavity problem. *International Journal of Numerical Methods for Heat & Fluid Flow* **10** (6), 598 – 615.

Niino, H., Mori, A., Satomura, T. & Akiba, S. 2006 Flow Regimes of Nonlinear Heat Island Circulation. *Journal of Atmospheric Sciences* **63**, 1538–1547.

Ogura, Y. & Phillips, N. A. 1962 Scale Analysis of Deep and Shallow Convection in the Atmosphere. *Journal of Atmospheric Sciences* **19**, 173–179.

Peng, Y.-F., Shiau, Y.-H. & Hwang, R. R. 2003 Transition in a 2-d lid-driven cavity flow. *Computers & Fluids* **32** (3), 337 – 352.

Pielke, R. A. 2002 *Mesoscale Meteorological Modeling*, 2nd edn. Academic press.

Press, W. H., Teukolsky, S. A., Vetterling, W. T. & Flannery, B. P. 2007 *Numerical recopies: the art of scientific computing*. Cambridge University Press.

Quere, P. L. 1991 Accurate solutions to the square thermally driven cavity at high rayleigh number. *Computers & Fluids* **20** (1), 29 – 41.

Saad, Y. & Schultz, M. H. 1986 Gmres: a generalized minimal residual algorithm for solving nonsymmetric linear systems. *SIAM J. Sci. Stat. Comput.* **7**, 856–869.

Skamarock, W., Oliger, J. & Street, R. L. 1989 Adaptive grid refinement for numerical weather prediction. *J. Comput. Phys.* **80**, 27–60.

Spiegel, E. A. & Veronis, G. 1960 On the Boussinesq Approximation for a Compressible Fluid. *Astrophysical Journal* **131**, 442–447.

Tannehill, J. C., Anderson, D. A. & Pletcher, R. H. 1997 *Computational fluid mechanics and heat transfer*, second edition edn. Taylor & Francis.

Vasilyev, O. V. & Bowman, C. 2000 Second-generation wavelet collocation method for the solution of partial differential equations. *J. Comput. Phys.* **165**, 660–693.

Vasilyev, O. V. & Kevlahan, N. K.-R. 2005 An adaptive multilevel wavelet collocation method for elliptic problems. *Journal of Computational Physics* **206** (2), 412 – 431.

van der Vorst, H. A. 2003 *Iterative krylov methods for large linear systems*, 1st edn. Cambridge university press.

Warming, R. F. & Hyett, B. J. 1974 The modified equation approach to the stability and accuracy analysis of finite-difference methods. *Journal of Computational Physics* **14** (2), 159 – 179.

Yang, X., Hou, Y. & Chen, B. 2011 Observed surface warming induced by urbanization in east china. *JOURNAL OF GEOPHYSICAL RESEARCH* **116**.